RICE UNIVERSITY

Searching For FFLO States in Ultracold Polarized Fermi Gases: A Numerical Approach

by

Hong Lu

A THESIS SUBMITTED
IN PARTIAL FULFILLMENT OF THE
REQUIREMENTS FOR THE DEGREE

Doctor of Philosophy In Physics

APPROVED, THESIS COMMITTEE

Dr. Han Pu, Associate Professor, Chair
Physics and Astronomy

Dr. Randall G. Hulet, Professor
Physics and Astronomy

Dr. Tim Warburton, Associate Professor
Computational and Applied Mathematics

HOUSTON, TEXAS
OCTOBER 2012

ABSTRACT

Searching For FFLO States in Ultracold Polarized Fermi Gases:

A Numerical Approach

by

Hong Lu

Ultracold atomic gases have emerged as an ideal laboratory system to emulate many-body physics in an unprecedentedly controllable manner. Numerous many-body quantum states and phases have been experimentally explored and characterized using the ultracold atomic gases, offering new insights into many exciting physics ranging from condensed matters to cosmology.

In this thesis, we will present a systematic numerical study of a novel experimental system, population imbalanced two-component ultracold Fermi gases. We explore the phase diagram of this system in both 3D and 1D especially focusing on the exotic Fulde-Ferrell-Larkin-Ovchinnikov (FFLO) phase, which is characterized by a spatially oscillating order parameter. In 3D, we solve for the stationary states of trapped imbalanced Fermi gases in a wide range of parameter space with a home-made parallel eigen-solver for Bogoliubov-de Gennes (BdG) equations. Our results show that there exists a metastable state with a FFLO type oscillating order parameter. In 1D, we simulate the dynamical expansion of the population imbalanced Fermi gases from the trap. A numerically quasi-exact scheme, time-evolving block decimation (TEBD), is introduced for the comparative studies with

the solution of the time-dependent BdG equation. Our results predict that the existence of FFLO states will leave conspicuous signatures in the density profiles during the expansion. For further understanding of the interplay between the population imbalance and two-body pairing interaction between two spin components, we also study the spin transport properties through trapped ultracold Fermi gases. The preliminary results will be discussed.

Acknowledgments

First and foremost I would like to thank my adviosr Prof. Han Pu who has opened the door of the exciting world of cold atomic physics to me. I am very honored to be one of his first two PhD students. He has contributed to all aspects of this work. I especially appreciate the timely help and inspiring guidance he has provided whenever our research runs into a roadblock. Without his patience and encouragement, this work would have been impossible for me to complete.

Also, I would like to extend my appreciation to Dr. Baksmaty, whom I have been working with during the entire time of my PhD studies. Without his help and guidance, it would have been extremely tough time for me to handle all the high-performance computatations involved in this work.

I also want to express my thanks to many other professors, colleagues and classmates at Rice for their friendship and support.

Contents

List of Figures

List of Tables

Chapter 1

Introduction

In the past decade, the field of cold atomic and molecular physics has witnessed an impressive amount of experimental progresses [1, 2, 3, 4, 5, 6] and consequently substantial theoretical efforts [7, 8] are being spent in understanding the experiments as well as in investigating underlying physics. Cold atoms provide people with systems amenable to exquisite experimental control. Experimentalists can tune the interaction strengths, confining potential geometries, and many other important parameters, which makes cold atomic gases a very attractive laboratory system to investigate the complicated physics compared with conventional electronic materials. With the observation of the superfluidity in ultracold Fermi gas, such systems are starting to become a promising 'quantum simulator' linking atomic physics to condensed matter physics. Superconductivity is one of the most challenging puzzles in condensed matter physics since early in last century. In the 1950s, people started to realize that pairing is the key to understand superfluidity and superconduc-

tivity when Cooper first time showed that, in the presence of a Fermi sea, two electrons with opposite spins can form a bound state at arbitrarily weak interaction strength [9]. Bardeen, Cooper and Schrieffer later proposed a theory based on a variational form of the ground state for the many-body system [10], which is now well known as the BCS theory of superconductivity. Later on, in the early 1980s, Nozieres, Schmitt-Rink and Leggett [11, 12] proposed the crossover picture between weakly attracting fermions described by the BCS mean-field theory to strongly attractive regime where molecular Bose-Einstein condensates (BECs) form in the system. The experimental confirmation was not available until the application of Feshbach resonance [13, 14] tuning the interaction in cold atom systems.

Let us start by considering a dilute ultracold mixture of fermions in two distinct hyperfine states. Such model systems are ideal and powerful tools for physicists to understand pairing mechanism and superconductivity by mimicking spin-1/2 electronic system. In such two-component ultracold Fermi gases, due to the Pauli exclusion principle and ultralow temperature, the interaction between the two hyperfine states are dominated by two-body scattering between unlike spins, which can be modeled using zero-range contact potential. The amplitude of two-body scattering can be formulated as $f(k) = -a/(1 + ika)$, where k is the relative momentum and a is called the scattering length, which characterizes the interaction in two-component Fermi gases. As we can see for a special case, when the scattering length diverges, i.e.$|a| \to \infty$, the scattering amplitude goes to a universal finite value $f = 1/ik$. This regime is called the unitary limit where the system is strongly interacting and the physical properties are independent of the microscopic details. On one side

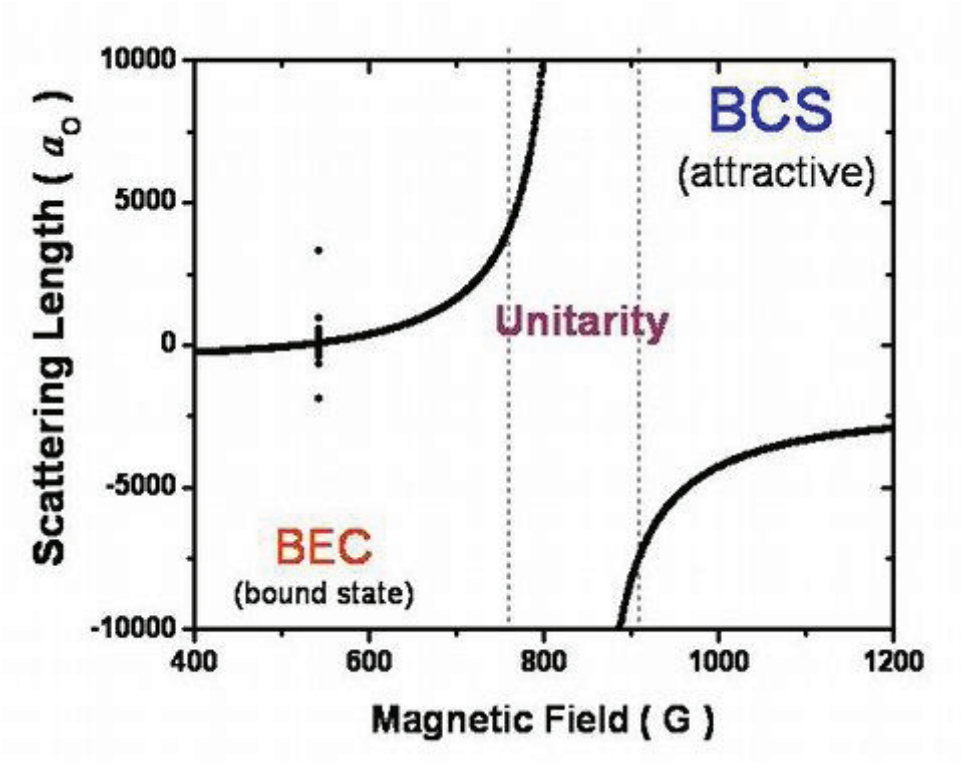

Figure 1.1: Feshbach Resonance of ^{6}Li atoms near 834G [16]

of unitary limit where $k_F a \to 0^+$, the system possesses a two-body molecular bound state. The tightly bound pairs are highly spatially correlated and can undergo Bose-Einstein condensation, therefore this is called the BEC limit. On the other side where $k_F a \to 0^-$, this corresponds to a weakly attractive regime called the BCS limit where system is highly momentum correlated and behaves as a condensate of Cooper pairs. The Feshbach resonance provides a knob to tune the scattering length in cold atoms [15], enabling experimentalists to observe a smooth crossover connecting all these states when the scattering length changes the sign by passing through the infinity. Fig. 1 shows a BEC-BCS crossover in ^{6}Li

.

Despite that the BCS theory successfully describes the pairing phenomena and resultant superfluidity and superconductivity in fermionic system, a natural question arises about the fate of the superconductivity when the system becomes spin polarized, i.e., the population of two spin components are unequal. In such a scenario, the majority component is necessarily partially unpaired, thus the system needs to configure itself into a new state to accommodate these unpaired fermions. This question was first investigated by Clogston [17] and Chandrasekhar [18]. Neglecting the orbital effects which induce the Meissiner effect in the superconductors, they considered the spin imbalanced system to be induced by Zeeman coupling between electronic spin and external magnetic field B and found a first order phase transition from superconductivity to normal state which happens at a certain magnetic field strength and this is referred to as the Clogston-Chandrasekhar (CC) limit. Various pairing mechanisms and exotic phases have been proposed for the polarized fermionic system. Among them, the most interesting one may be the FFLO state suggested by Larkin,Ovchinnikov (LO) [19]and Fulde and Ferrel (FF) [20]. The idea was based on a simple argument as follows: because BCS wavefunction cannot accommodate finite momentum into Cooper pair, the Fermi surface of the two spin species would move towards to each other and become closer in one direction. This may lead to a spatially varying order parameter $\triangle(\mathbf{r})$. It is worth noting that there is some subtle difference between FF's proposal and LO's. In FF's proposal, they suggested a homogeneous order parameter with phase modulation:

$$\triangle(\mathbf{r})_{FF} = \triangle e^{i\mathbf{q}.\mathbf{r}} \tag{1.1}$$

where $\mathbf{q} = \mathbf{k}_F^{\uparrow} - \mathbf{k}_F^{\downarrow}$ is the finite center of mass momentum, $\mathbf{k}_F^{\uparrow}, \mathbf{k}_F^{\downarrow}$ are the Fermi vectors for spin ↑ and ↓ particles. LO proposed a spatially modulated order parameter

$$\triangle(\mathbf{r})_{LO} = \triangle(e^{i\mathbf{q}.\mathbf{r}} + e^{-i\mathbf{q}.\mathbf{r}}) = \triangle\cos(\mathbf{q} \,.\, \mathbf{r}) \tag{1.2}$$

There have been exhaustive experimental efforts to search for this exotic pairing state in condensed matter systems, while it is still elusive from direct observation except for some ambiguous evidences from heavy fermion [21] and organic [22, 23] superconductors systems. The polarized Fermi gases enable people to continue this search with a more controllable manner because cold atoms have longer spin relaxation time compared against the conventional condensed matter systems. The spin imbalance therefore can be created with radio-frequency field or optical pumping in cold atoms and kept for a long time for experimental observations. In 2006, two groups at Rice and MIT experimentally realized 3D ultracold polarized Fermi gases at unitarity. While some features of the observations fall into theorists' expectations, there are significant discrepancies between the results from these two groups and the direct signature of FFLO state is missing.

Another crucial factor for successfully observing the FFLO state in the experiments is the dimensionality of the system, which plays an important role in stabilizing the FFLO states as have been found in condensed matter systems. It has been predicted [24] that in 3D polarized Fermi gases, stable FFLO state may occupy little of parameter space, while it could become dominant in phase diagram in 1D due to the analogous of 'nesting' effects in charge density waves and spin density waves [25]. In 2010, the Rice group successfully realized the polarized Fermi gases in 1D [26], which opens a door to the search for the

FFLO states. However, the static density profile in the trap does not show the smoking gun's signature of the existence of the FFLO states.

The aim of this thesis is to present our work in seeking FFLO state in both 3D and 1D polarized ultracold Fermi gases using numerical simulations. These studies are closely related to the recent experimental advancements, especially at Rice university. Although a lot of theoretical efforts are being devoted to the study of ultracold Fermi gases, much is conducted by analytical or semi-analytical means, with the whole range of quantum statistical tools. As it always happens to the case of complex physical phenomena, analytical methods face severe limitations whenever genuinely non-perturbative and strongly nonlinear effects in realistic experiments need to be quantitatively addressed. Under these circumstances, numerical measures become indispensable. Particularly in ultracold quantum gases, since all experiments are necessarily performed in the presence of trapping potentials that hold the atoms together, inhomogeneity and finite-size effect prevent a lot of well-developed analytical approaches from giving accurate descriptions of such systems. Therefore, this thesis is organized into two parts for 3D and 1D polarized Fermi gases respectively: In Chapter 2, we will discuss about our efforts to seek FFLO states in 3D elongated trapped polarized Fermi gases using mean-field Bogoliubov-de Gennes (BdG) approach. The results reprented there have been previously published in the Ref. [27, 28]. In Chapter 3, we move forward from 3D to 1D while extending our scope from static ground state to the expansion dynamics of the partially polarized Fermi gases. In this study, besides implementing a time-dependent BdG solver, we introduce the time-evolving block decimation

(TEBD) algorithm, a 'quasi-exact' numerical method suitable for studying the dynamics of 1D strongly correlated systems. Our results, using the combination of these two approaches, suggest that during the expansion, the existence of FFLO phase would cause strong peaks in density profile for direct observation. The majority of these results have been previously published in the Ref. [29]. The TEBD method furnishes us with an efficient and accurate measure studying the dynamical processes in 1D systems. With reference to this advantage, we close with a preliminary numerical experiment of spin transportation to investigate the interplay between the pairing and the population imbalance.

Chapter 2

BdG studies of trapped polarized Fermi gases in 3D at unitary

2.1 Introduction

In this Chapter, we present our efforts in understanding ground states and metastability of ultracold polarized Fermi gases in the unitary regime by using scalable numerical techniques which take full advantage of cutting-edge high-performance computing facilities running parallel codes over thousands of CPUs. Our investigation was in the first place motivated by the apparently contradictory results from recent experiments between two groups [30, 31, 32, 33, 34, 35]. In both experiments it was observed that the trapped superfluid responds to polarization by phase separating into an inner core with negligible polarization surrounded by a polarized outer shell. However, the Rice experiments [34, 35]

performed in cigar-shaped traps with total particle numbers $N \sim 10^5$ observed a significant and unexpected deformation of the central superfluid core, indicating a clear violation of the prediction based on the so-called local density approximation (LDA) method. In addition, the results from Rice experiment also suggest a much higher superfluid to normal CC transition than the MIT experiments [30, 31] in which no deformations were observed. The excellent quantitative agreement with theory [36, 37, 38, 39] in the MIT experiments, conducted at much lower trap aspect ratio and with higher particle numbers $N \sim 10^6$, hints that there might be unexpected physics at work in the Rice experiment. In addition, the concurrence of experiments performed in Paris [40] with the MIT experiments also suggest a crucial role of the trapping geometry. This impasse has inspired speculations about the possible role of exotic phases such as the FFLO state in the observed discrepancies.

The apparent discrepancies between the Rice and MIT experiments reflect theoretical difficulties in understanding the effects of trapped geometries in cold atom experiments. In order to extract the bulk properties of the system (e.g, the equations of state) from measurement on a trapped sample of cold atoms, LDA, as a typical theoretical method, is widely adopted to account for the spatial imhomogeneousity in the system. Briefly the LDA assumes the system is locally homogenous as a part of an infinite system and the spatially varying trapping potential will be absorbed into a local chemical potential $\mu(\mathbf{r}) \longrightarrow \mu - V(\mathbf{r})$. The LDA can be seen as an accurate approximation for large particle number N without the presence of phase boundaries. However, if large change in the density occurs, in our case, from the center to the edge of the trap which indicates multiple phases coexist in the

system , then care needs to be taken when applying the LDA method. Especially when the number of particles in the sample is small and finite-size effects are significant, the corrections to the LDA results become crucial even when only one phase is present in the trapped sample [41]. Furthermore, the LDA method cannot correctly take into account the surface energy correction due to the shape of the distortions [42, 43, 44]. Thus, the LDA is not an adequate approach to capture exotic phases such as the FFLO states. To this end we employ an approach by self-consistently solving Bogoliubov-de Gennes (BdG) equations [45], which is a powerful mean-field tool particularly suitable for inhomogeneous Fermi superfluids, and has been recently adopted by many to study trapped ultra-cold Fermi gases [39, 46, 47, 48, 49] .

Overall, our calculation will serve two purposes: first, we want to examine the validity of the LDA as the particle number and aspect ratio of the trap are varying. The second aim is closely related to the new development in interpreting the observations in the Rice experiment. Recently Parish et.al [50], after carefully examining the detailed setup of the Rice experiment, proposed that the LDA-violating deformation observed could be a result of depolarization of the superfluid core by evaporation occurring mainly at the axial center of the trap. Later on this proposal has been experimentally verified by the Rice group [51]. According to [50], the evaporative cooling at the center shortens the ellipsoidal partially polarized region along the major axis where the condensate forms and leads to the observation of possibly metastable states in the experiment. This led us to investigate the metastability of these states by constructing initial ansatz imitating this circumstance and

compare the calculated final states with the results from the Rice experiment directly.

2.2 Hybrid Mean-Field BdG Strategy

2.2.1 Formalism of BdG equations

The system we consider is a gas of $N = N_\uparrow + N_\downarrow$ spin-polarized fermionic atoms interacting through a contact potential ($g \sum_{i<j} \delta^3(\mathbf{R_i} - \mathbf{R_j})$) and confined to a harmonic trap defined in cylindrical coordinates (ρ, ϕ, z) by $V_{\text{ext}}(\mathbf{R}) = \frac{m}{2}(\omega_\perp^2 \rho^2 + \omega_z^2 z^2)$ with axial and radial frequencies denoted by $(\omega_z, \omega_\perp)$. In addition to the total number N, we define the total polarization of the cloud $P = (N_\uparrow - N_\downarrow)/(N_\uparrow + N_\downarrow)$, which can be varied through independent control of the number of particles in each spin projection N_σ,$\sigma = (\uparrow, \downarrow)$. We work at unitarity ($a_s \to \infty$) and within a cigar-shaped trap with the aspect ratio $\alpha = \omega_\perp/\omega_z$. This system of $N = N_\uparrow + N_\downarrow$ atoms interacting through contact interaction is described by a Hamiltonian $\hat{H} = \int d\mathbf{R}\,(H_0 + H_I)$ with non-interacting H_0 and interacting H_I portions given by:

$$\begin{aligned} H_0(\mathbf{R}) &= \sum_\sigma \psi_\sigma^\dagger(-\frac{\hbar^2}{2m}\nabla^2 + V_{\text{ext}}(\mathbf{R}) - \mu_\sigma)\psi_\sigma, \\ H_I(\mathbf{R}) &= g\,\psi_\uparrow^\dagger(\mathbf{R})\psi_\downarrow^\dagger(\mathbf{R})\psi_\downarrow(\mathbf{R})\psi_\uparrow(\mathbf{R}), \end{aligned} \tag{2.1}$$

where $\psi_\sigma(\mathbf{R})$ represents the fermionic field operators, m the mass and μ_σ the chemical potential of atomic species with spin σ. The coupling constant is defined as $g = \frac{4\pi\hbar^2 a_s}{m}$. Henceforth, we work in trap units for which: $m = \omega_z = \hbar = k_B = 1$. This implies that energies will be measured in units of $\hbar\omega_z$, lengths in units of $l_0 = \sqrt{\frac{\hbar}{m\omega_z}}$ and temperature (T) in units of $\hbar\omega_z/k_B$.

We will treat the Hamiltonian (2.1) within the mean-field BdG formalism [45] which has been adopted in studying many fermionic systems. However, to build a practical numerical scheme to solve the BdG equations, we employ a hybrid structure [39] combining low-lying eigenmodes of BdG equation and semi-classical LDA for high-lying modes above a carefully chosen energy cutoff E_c.

We would like to devote a few lines here to comment on the validity of the BdG theory at unitarity because it is expected that quantum fluctuations and other effects due to the strong interactions could be significant in this regime. The main drawbacks of the BdG formalism is that it fails to account for phase fluctuations. At unitarity it has an additional disadvantage in that it also fails to account for interactions within the normal fluid which is unitarity limited [52]. However the BdG is widely expected to yield qualitatively reliable answers for two main reasons. First, because of the finite size of these experiments, the trapped gas enjoys protection from fluctuations of arbitrarily low energy or of very long wavelengths. Secondly, due to experimental evidence for superfluidity at unitarity, it is quite clear that interactions within the normal fluid are not so great that the order parameter cannot form or will be destroyed. Thus, the failure to account for these effects is not expected to change the topology of the phase diagram but at most would slightly shift the phase boundaries. Since our purpose to examine the suitability of the LDA is qualitative, we are confident that the BdG can account for the essential physics. Nevertheless, due to the limitations within the BdG formalism, in particular the neglect of interaction in the normal fluid, our calculation fails to quantitatively locate the position of the Clogston limit.

In addition, it cannot be applied to study a system with extremely large polarization (i.e., $P \approx 1$) where the polaron physics will dominate [40, 53].

2.2.2 BdG formalism for low-lying state

In this section, we present the BdG formalism we employed for states below the cutoff energy E_c, which closely follows the derivation presented in Ref. [39]. We first apply mean field approximation on the interacting Hamiltonian, and define mean-field quantities, the pairing field or gap parameter $\Delta(\mathbf{R})$ as following:

$$\Delta(\mathbf{R}) = -g\langle\psi_\downarrow(\mathbf{R})\psi_\uparrow(\mathbf{R})\rangle, \tag{2.2}$$

and the mean-field interacting Hamiltonian can be expressed as

$$H_I(\mathbf{R}) = -\mathbf{\Delta}\psi^\dagger_\uparrow(\mathbf{R})\psi^\dagger_\downarrow(\mathbf{R}) - \mathbf{\Delta}^*\psi_\uparrow(\mathbf{R})\psi_\downarrow(\mathbf{R}) \tag{2.3}$$

By introducing the Nambu spinor $\Psi(\mathbf{R}) = [\psi_\uparrow(\mathbf{R}), \psi^\dagger_\downarrow(\mathbf{R})]^\mathbf{T}$, we can derive the effective mean-field Hamiltonian as:

$$\mathcal{H}_{\text{eff}} = \int d\mathbf{R}\, \Psi^\dagger(\mathbf{R}) \begin{bmatrix} H^s_\uparrow(\mathbf{R}) & \Delta(\mathbf{R}) \\ \Delta^*(\mathbf{R}) & -H^s_\downarrow(\mathbf{R}) \end{bmatrix} \mathbf{\Psi}(\mathbf{R}) \tag{2.4}$$

where the single particle Hamiltonian

$$H^s_\sigma(\mathbf{R}) = -\nabla^2/2 + V_{\text{ext}}(\mathbf{R}) - \mu_\sigma. \tag{2.5}$$

$\mathcal{H}_{\text{eff}}$ can be diagonalized into the form $\mathcal{H}_{\text{eff}} = \sum_{j,\sigma} E_{j,\sigma}\eta^\dagger_{j,\sigma}\eta_{j,\sigma}$, where $\eta^\dagger_{j,\sigma}$ and $\eta_{j,\sigma}$ are the creation and annihilation operators of the quasi-particles, which obey the fermionic

commutation relations. For this purpose, we change the Nambu spinor into the quasi-particle basis $\eta_j \equiv [\eta_{j,\uparrow}, \eta^{\dagger}_{j,\downarrow}]^T$ using the Bogoliubov transformation, which is defined by

$$\Psi(\mathbf{R}) = \sum_{\mathbf{j}} \begin{bmatrix} u_{j,\uparrow}(\mathbf{R}) & -v^*_{j,\downarrow}(\mathbf{R}) \\ v_{j,\uparrow}(\mathbf{R}) & u^*_{j,\downarrow}(\mathbf{R}) \end{bmatrix} \eta_{\mathbf{j}} \tag{2.6}$$

Thus we obtain the BdG equations for the pair wave functions $u_{j,\sigma}(\mathbf{R})$ and $v_{j,\sigma}(\mathbf{R})$ with the corresponding eigenvalues $E_{j,\sigma}$ as follows:

$$\begin{bmatrix} H^s_\sigma & \Delta(\mathbf{R}) \\ \Delta(\mathbf{R}) & -H^s_{\bar{\sigma}} \end{bmatrix} \begin{bmatrix} u_{j,\sigma}(\mathbf{R}) \\ v_{j,\sigma}(\mathbf{R}) \end{bmatrix} = E_{j,\sigma} \begin{bmatrix} u_{j,\sigma}(\mathbf{R}) \\ v_{j,\sigma}(\mathbf{R}) \end{bmatrix} \tag{2.7}$$

In accordance with fermionic commutation relations [45], the $u_{j,\sigma}(\mathbf{R})$ and $v_{j,\sigma}(\mathbf{R})$ are normalized as

$$\int d\mathbf{R} \left(|u_{j,\sigma}(\mathbf{R})|^2 + |v_{j,\sigma}(\mathbf{R})|^2\right) = 1 \tag{2.8}$$

and are related to the spin densities through :

$$n_\sigma(\mathbf{R}) = \frac{1}{2} \sum_j \left[\left|u_{j\sigma}\right|^2 f\left(E_{j\sigma}\right) + \left|v_{j\bar{\sigma}}\right|^2 f\left(-E_{j\bar{\sigma}}\right) \right] \tag{2.9}$$

where $f(E) = 1/(e^{E/k_B T} + 1)$ is the Fermi-Dirac distribution function at temperature T. The paring field or gap paramter is given by

$$\Delta(\mathbf{R}) = \frac{g}{2} \sum_j \left[v^*_{j\uparrow} u_{j\uparrow} f\left(E_{j\uparrow}\right) - u_{j\downarrow} v^*_{j\downarrow} f\left(-E_{j\downarrow}\right) \right] \tag{2.10}$$

Furthermore, the above BdG equation (2.7) can be simplified by noticing that the solutions for two spin components always emerge in pairs as follows,

$$E_{j\sigma} \leftrightarrow -E_{j\bar{\sigma}}, \tag{2.11}$$

and

$$\begin{bmatrix} u_{j\sigma}(\mathbf{R}) \\ v_{j\sigma}(\mathbf{R}) \end{bmatrix} \leftrightarrow \begin{bmatrix} -v^*_{j\bar{\sigma}}(\mathbf{R}) \\ +u^*_{j\bar{\sigma}}(\mathbf{R}) \end{bmatrix}. \tag{2.12}$$

Therefore, we only need to solve the BdG equation for one spin component. After removing the spin index from the Eq. (2.7), we obtain the simplified equation as follows:

$$\begin{bmatrix} H^s_\uparrow & \Delta(\mathbf{R}) \\ \Delta(\mathbf{R}) & -H^s_\downarrow \end{bmatrix} \begin{bmatrix} u_j(\mathbf{R}) \\ v_j(\mathbf{R}) \end{bmatrix} = E_j \begin{bmatrix} u_j(\mathbf{R}) \\ v_j(\mathbf{R}) \end{bmatrix}, \tag{2.13}$$

Correspondingly, the normalization and spin densities and gap parameter have a new form in u_j and v_j,

$$\int d\mathbf{R}\,(|u_{j,\sigma}(\mathbf{R})|^2 + |v_{j,\sigma}(\mathbf{R})|^2) = 1 \tag{2.14}$$

$$\begin{aligned} \rho_\uparrow(\mathbf{R}) &= \sum_{j=1} |u_j(\mathbf{R})|^2 f(E_j), \\ \rho_\downarrow(\mathbf{R}) &= \sum_{j=1} |v_j(\mathbf{R})|^2 f(E_j). \end{aligned} \tag{2.15}$$

and

$$\Delta(\mathbf{R}) = -g\langle\psi_\uparrow(\mathbf{R})\psi_\downarrow(\mathbf{R})\rangle = -g\sum_j u_j(\mathbf{R})v^*_j(\mathbf{R})f(E_j) \tag{2.16}$$

Eqs. (2.13), (2.14) and (2.16) constitute a closed set of nonlinear equations which can be solved self-consistently.

However, using the contact potential will lead to ultraviolet divergence in 3D because the contact interaction assumes wrongly that all states are scattered in the same way regardless of their incoming energy and consequently sums in contributions from collisions at arbitrarily high energy. Hence the gap equation (2.16) needs to be properly regularized. The renormalization process is described in Appendix A.

2.2.3 LDA treatment above cutoff

In order to ensure accuracy, as previously stated, an energy cutoff E_c is introduced, such that in the sum of Eq. (2.16), only modes with $|E_j| < E_c$ are included. To incorporate the contribution from states above the energy cutoff, we follow the hybrid scheme derived in Ref. [39]. For $|E_j| > E_c$, we adopt the LDA formalism, which keeps only the leading order of the pair wave function $u_j(\mathbf{R})$ and $v_j(\mathbf{R})$ in the BdG equations as follows:

$$\begin{aligned} u_j(\mathbf{R}) &\rightarrow u(\mathbf{k},\mathbf{R})\exp\left[\mathbf{ik}\cdot\mathbf{R}\right], \\ v_j(\mathbf{R}) &\rightarrow v(\mathbf{k},\mathbf{R})\exp\left[\mathbf{ik}\cdot\mathbf{R}\right], \\ E_j &\rightarrow E\left(\mathbf{k}\right), \end{aligned} \tag{2.17}$$

the BdG equation becomes

$$\begin{bmatrix} H^s_{\uparrow}(\mathbf{k},\mathbf{R}) & \Delta(\mathbf{R}) \\ \Delta(\mathbf{R}) & -H^s_{\downarrow}(\mathbf{k},\mathbf{R}) \end{bmatrix} \begin{bmatrix} u_k \\ v_k \end{bmatrix} = E(\mathbf{k}) \begin{bmatrix} u_k \\ v_k \end{bmatrix} \tag{2.18}$$

where

$$H^s_{\sigma}\left(\mathbf{k},\mathbf{R}\right) = k^2/2 + V_{\text{ext}}(\mathbf{R}) - \mu_{\sigma} \tag{2.19}$$

It is easy to see that the equation has two branches of solutions as follows,

$$E\left(\mathbf{k},\pm\right) = E_{\mathbf{k}} \mp \delta\mu \tag{2.20}$$

where $E_{\mathbf{k}} = \left[\xi^2_{\mathbf{k}} + \Delta^2(\mathbf{R})\right]^{1/2}$ and $\xi_{\mathbf{k}} = \hbar^2k^2/2m + V_{\text{ext}}(\mathbf{R}) - \mu$. The corresponding eigenfunctions for the two branch solutions are, respectively,

$$u^2_{\mathbf{k}} = \frac{1}{2}\left(1 + \frac{\xi_{\mathbf{k}}}{E_{\mathbf{k}}}\right),\ v^2_{\mathbf{k}} = \frac{1}{2}\left(1 - \frac{\xi_{\mathbf{k}}}{E_{\mathbf{k}}}\right),\ u_{\mathbf{k}}v^*_{\mathbf{k}} = +\frac{\Delta(\mathbf{R})}{2E_{\mathbf{k}}}. \tag{2.21}$$

and

$$u_{\mathbf{k}}^2 = \frac{1}{2}\left(1 - \frac{\xi_{\mathbf{k}}}{E_{\mathbf{k}}}\right),\ v_{\mathbf{k}}^2 = \frac{1}{2}\left(1 + \frac{\xi_{\mathbf{k}}}{E_{\mathbf{k}}}\right),\ u_{\mathbf{k}} v_{\mathbf{k}}^* = -\frac{\Delta(\mathbf{R})}{2E_{\mathbf{k}}}. \tag{2.22}$$

When the energy cutoff is sufficiently high ($E_c/k_BT \gg 1$, i.e. $f(E > E_c) = 1.$), which is the case in our calculation, the above cutoff contribution for density and gap parameter can be simplified as follows:

$$n_{\uparrow,\mathrm{LDA}}(\mathbf{R}) = \sum_{E(\mathbf{k},-)>Ec} \frac{1}{2}\left(1 - \frac{\xi_{\mathbf{k}}}{E_{\mathbf{k}}}\right), \tag{2.23}$$

$$n_{\downarrow,\mathrm{LDA}}(\mathbf{R}) = \sum_{E(\mathbf{k},+)>Ec} \frac{1}{2}\left(1 - \frac{\xi_{\mathbf{k}}}{E_{\mathbf{k}}}\right), \tag{2.24}$$

and

$$\Delta_{\mathrm{LDA}}(\mathbf{R}) = U \sum_{E(\mathbf{k},-)>Ec} \left[-\frac{\Delta(\mathbf{R})}{2E_{\mathbf{k}}}\right]. \tag{2.25}$$

2.2.4 Numerical Implementation

We discretize the BdG equation using a linear triangular finite element mesh in the ρ-z plane which anticipates that our results will retain the cylindrical symmetry of the confining potential V_{ext}. The accuracy of these calculations are controlled by the density of the trianglular mesh and the cutoff E_c used in the hybrid scheme. Both of these are changed in successive solutions until the free-energy or relevant observable converges to a sufficient accuracy. Experience has taught us that this simple renormalization scheme typically converges when the cutoff is of the order $6E_F$ (where E_F is the Fermi energy) which implies that the number of quasiparticle states to be directly calculated by Eq. (2.13) is about $6N$.

Note that this puts a constraint on the density of the discretizing mesh. Thus, for moderate system sizes, we are still presented with a very large problem. For example, for $N \sim 10^3$ particles, one essentially needs to calculate $\sim 10^4$ quasiparticle states at each iteration.

One important consequence of our finite element discretization is that it yields sparse matrices which are suitable to massively parallel matrix computations. This is of key importance given that the slow convergence of the gap function condemns us to calculate a very large number of quasi-particle states. This is true inspite of our efficient hybrid scheme, without which calculation would be prohibitive. It is immediately obvious that these difficulties will increase with the number of particles N, and will make the problem impractical for even moderate particle numbers without very careful formulation. In our case these difficulties are inescapable since the issues to be addressed occur in the presence of finite size effects and confinement. Hence, it was crucial to develop the ability to perform calculations with realistic particle numbers because it is not *a priori* obvious how physical properties will scale with system size. At each iteration, we need to find a large number of eigenvalues and eigenfunctions for large matrices. To this end, based on shift-and-invert scheme [54], we solve the BdG equation using a parallel eigen-solver we developed independently but is very similar to the one described in Ref. [55].

Briefly, the scheme involves partitioning the sought spectrum amongst groups of processors working independently. The size of the group is determined by the minimum number of processors with enough total memory to store the inverted matrix which is required for building the local Krylov basis. The main challenge here is bookkeeping to prevent

over-counting of states and balancing the load amongst the processor groups. It is conceivable that this method could have issues in cases where the equations support huge degenerate subspaces. In our particular formulation we exploited cylindrical symmetry and parity along the long trap axis to reduce the problem. Consequently we only had to contend with accidental degeneracies. We note here that this parallelization scheme is very efficient on distriubted computing systems and scales easily to thousands of CPU's which is as high as we have tested. Potentially it can be used to study much larger systems than we have reported in this thesis.

2.2.5 Summary of the algorithm

To provide a straightforward overview of the structure of the code, we put it into a flow chart as in Fig. 2.1.

As shown in the flow chart, the program will:

1. start with an initial guess of the order parameter $\Delta(\mathbf{R})$ such as the LDA result or a previously calculated state,

2. discretize the BdG equation over a fine enough finite element mesh, which is chosen on a self-consistent basis,

3. solve the BdG equation for all the states up to the chosen energy cutoff to find $u_j(\mathbf{R})$ and $v_j(\mathbf{R})$ using the shift-and-invert iterative solver,

4. update density and gap profiles and then adjust the chemical potentials $\mu_\uparrow$ and $\mu_\downarrow$

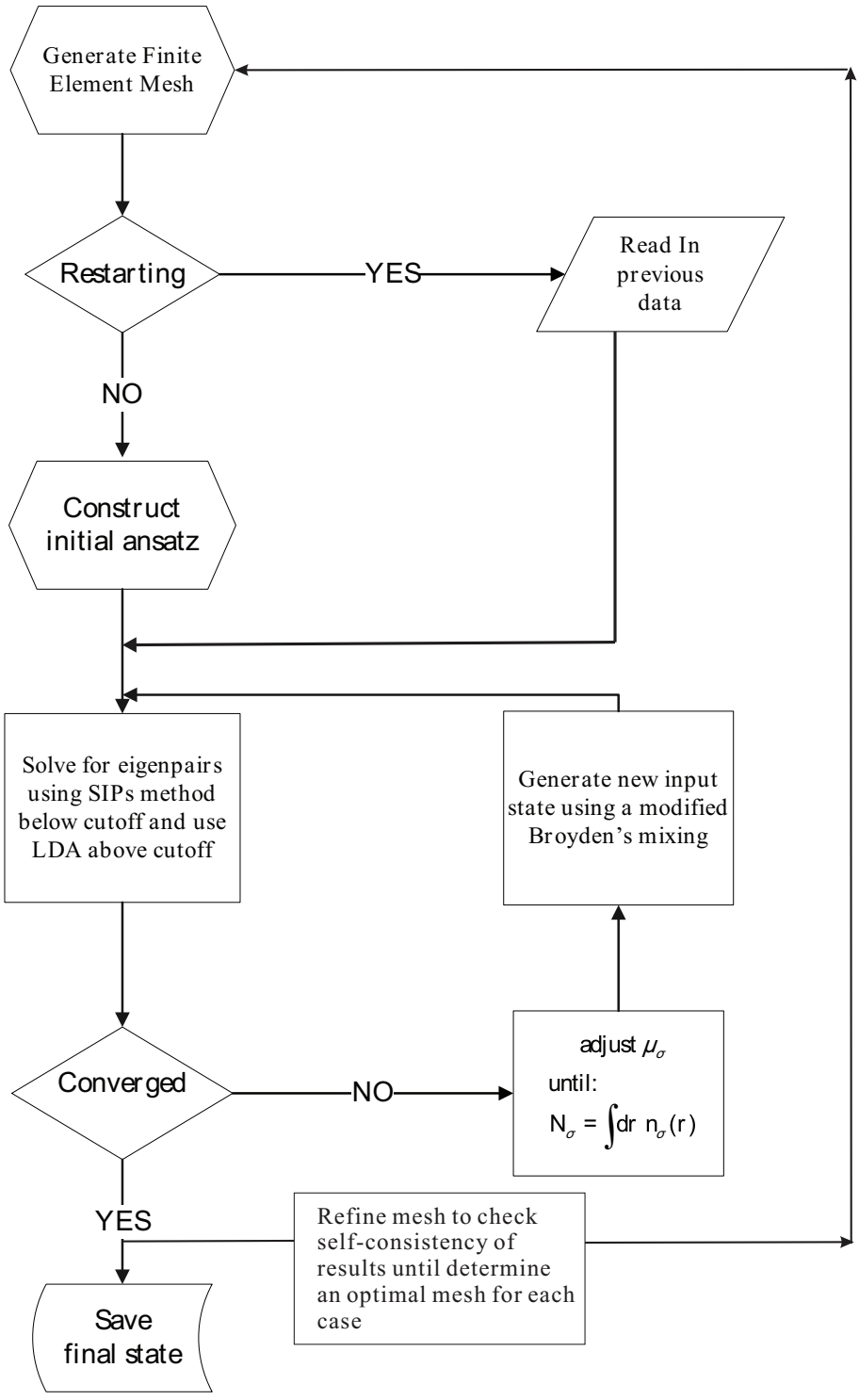

Figure 2.1: The basic flow of the code solving BdG equation self-consistently

under the conserved number of particles constraint,

5. generate new states using a modified Broyden's mixing method [56] to improve the self-consistency of the alogrithm until the calculation is converged to a steady state.

6. for specified particle number N and trap aspect ratio α, to ensure the accuracy of the eigen-solutions obtained, we repeat above steps on a refined finite element mesh, check the self-consistency of the results and determine an optimal mesh for the following calculations.

2.3 Results and discussions

With our home made powerful BdG solver, we were able to perform a systematic study of trapped polarized fermi gases with varying characteristic parameters such as total particle number, trap aspect ratio, and polarization. We search extensively in a large parameter space to charactize the effect of trap geometry and manifest the signature of FFLO states in experimental observations. Briefly, we can categorize our results into two classes by starting from different initial ansatz. The first class of solutions has a structure similar to that of LDA solution and is consistently the lowest in energy within our analysis, while the second class of solutions has a tendency towards metastable behavior as the trap becomes increasingly elongated. This could lead to the observation of states that are not necessarily the ground state.

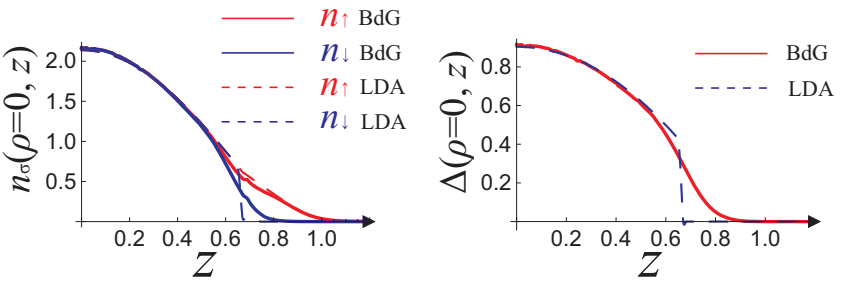

Figure 2.2: Density (left) and order parameter (right) profiles along the axial axes in a spherical trap, showing both BdG and LDA results

2.3.1 A case study for $N = 200$

We first choose a relatively small particle number of $N = 200$. As we will show, the system is rather sensitive to the trap geometry. In the following section, we first briefly discuss the case of a spherical trap with $\alpha = 1$ and then concentrate on elongated cigar-like trapping potentials with $\alpha > 1$ and then discuss them in detail. In all calculations, we adopted the LDA state as the intial ansatz to obtain the BdG results.

Spherical trap

To benchmark our work, we first did a confirmatory calculation for spherical trap geometry and found our results in perfect agreement with those reported in Ref. [39]. In this case, even though we anticipate only cylindrical geometry, the density profiles always obey the spherical symmetry. Note that the authors of Ref. [39] solved the one-dimensional (1D) radial equation, hence the spherical symmetry of the cloud is automatically imposed. We refer the readers to Ref. [39] for details, here we just briefly present the key features as shown in Fig. 2.2. The density profiles indicate a phase-separation scenario: a fully paired

BCS superfluid core at the trap center surrounded by a fully polarized shell composed of excess majority spins. A thin layer of partially polarized gas forms the interface between the superfluid core and the normal shell. In this intermediate regime, the minority density and the order parameter sharply drop to zero. Here and in other cases, we always found that the profile of the order parameter closely follows that of the density of the minority spin component. Furthermore, in this case, the LDA gives very good agreement with the full BdG calculation even for particle numbers as small as a few hundred.

Cigar trap

In practice, all the experiments on spin-imbalanced Fermi gases have been performed in cigar-like traps with aspect ratio $\alpha > 1$. Figure 2.3 illustrates several examples of the density profiles for $N = 200$ atoms confined in a moderately elongated trap with $\alpha = 5$, which is a trap aspect ratio close to what has been used in the MIT experiments. We express our results in terms of the Fermi energy $E_F = (3N)^{1/3}\alpha^{2/3}$, central number density $(2E_F)^{3/2}/(6\pi^2)$, and the Thomas-Fermi radius along the z-axis $Z_F = \sqrt{2E_F}$ for a single species ideal Fermi gas of $N/2$ particles in a trap with identical parameters. The upper row of Fig. 2.3 shows the density profiles of a system with a relatively small polarization $P = 0.2$. Here the axial spin density $\delta\rho_{1d}(z)$ exhibits a double-horn structure and vanishes near $z = 0$. This is a clear violation of the LDA which predicts that $\delta\rho_{1d}(z)$ should be flat topped [57]. Fig. 2.3 can be examined in tandem with Fig. 2.4 where upon closer inspection, we plot the densities and the order parameter along the axial and radial axis for

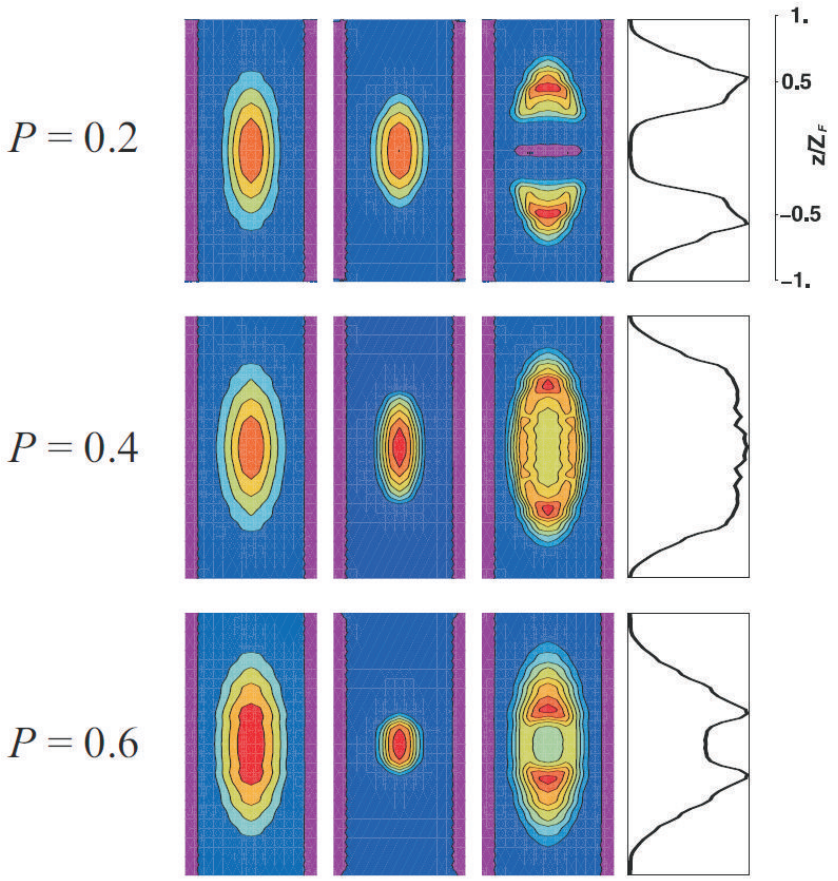

Figure 2.3: Density profile of the atomic cloud for $N = 200$ in an elongated trap with aspect ratio $\alpha = 5$. Adopted from Ref. [27]. The upper, middle and lower row are results from different polarizations $P = 0.2$, 0.4 and 0.6, respectively. In each row, we have shown (from left to right) the column densities of the majority component $\int dx \rho_\uparrow$, the minority component $\int dx \rho_\downarrow$, their difference $\int dx (\rho_\uparrow - \rho_\downarrow)$, and the axial spin density $\delta\rho_{1d}(z) = \int dxdy (\rho_\uparrow - \rho_\downarrow)$.

two different polarizations. Fig. 2.4(a) displays results for $P = 0.2$. The density profiles along the z-axis show clearly a phase separated three-region structure — moving from the center to the edge of the trap, we encounter a fully paired superfluid core, a partially paired intermediate region and a fully polarized normal gas, just like in the previous case of spherical trap. In stark contrast, the density profiles for the two components along the ρ-axis are completely overlapped. In fact, this matching of the radial profiles occur for $|z| \leq 0.1$. As a consequence, the axial spin density vanishes near $z = 0$ as shown in the upper row of Fig. 2.3.

That the majority and minority densities overlap along the radial direction can be understood from an argument invoking the surface energy. When induced phase separation occurs, there is an accompanying surface energy associated with the interface between the two phases. The system will then try to minimize the interface in order to reduce the associated energy. For a cigar-like trap as we study here, the superfluid-normal gas interface area can be efficiently reduced if the two spin components match their densities radially. The authors of Ref. [42, 43] devised phenomenological theories to include the surface term variationally to explain the breakdown of the LDA observed in the Rice experiment [34, 35]. In our calculation, the surface energy is automatically included from the self-consistent BdG formulation [58].

As polarization increases, eventually it becomes energetically unfavorable to have this radial overlap. This is illustrated in Fig. 2.4(b) for $P = 0.6$. Consequently, the axial spin density no longer vanishes near $z = 0$ and the LDA becomes more accurate (see the

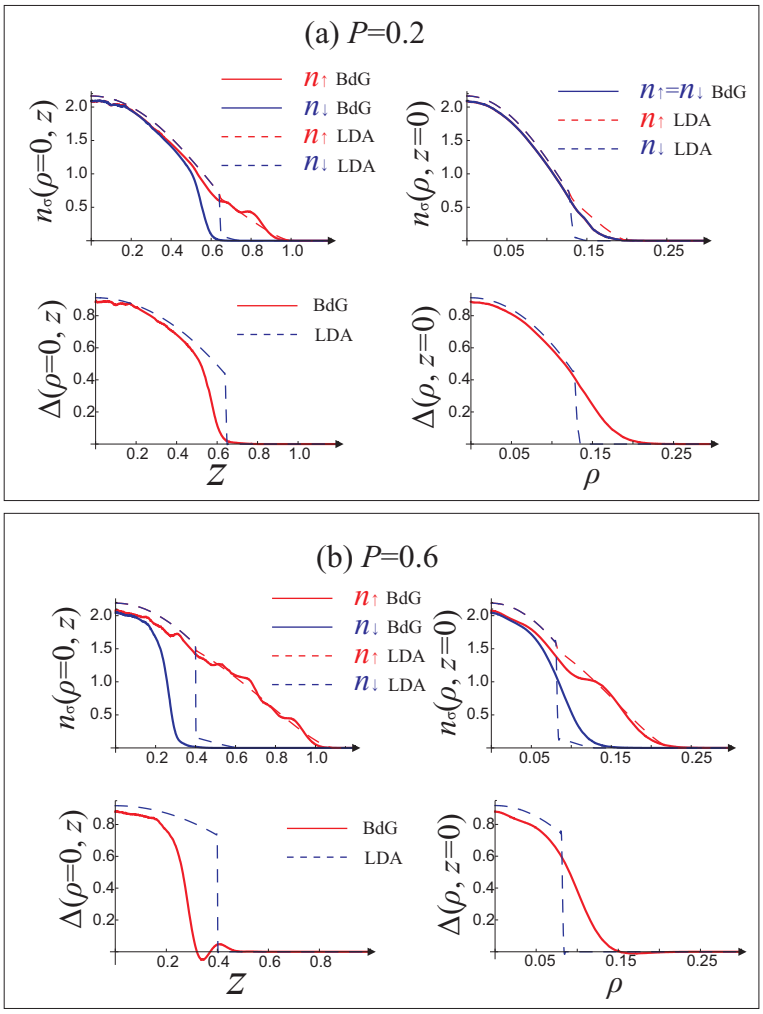

Figure 2.4: Density and order parameter profiles along the axial and radial axes in a cigar-like trap with $\alpha = 5$ for two differnet polarizations: (a) $P = 0.2$ and (b) $P = 0.6$. Adopted from Ref. [27].

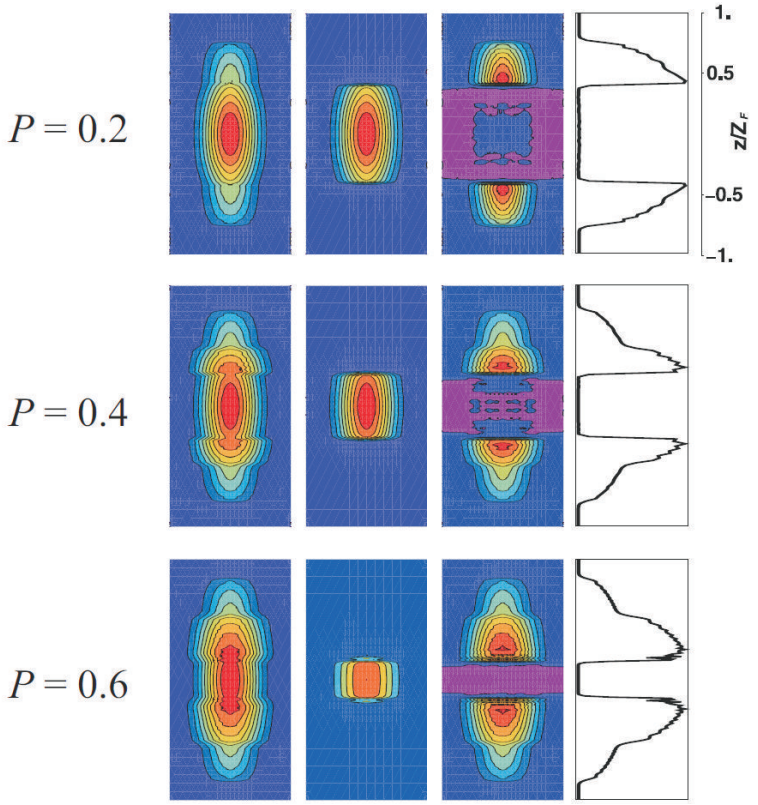

Figure 2.5: Same as in Fig. 2.3, but for $\alpha = 50$, Adopted from Ref. [27].

middle and bottom rows of Fig. 2.3). In addition, it is quite noticeable that, particularly for large P, the minority component density has a steeper down turn along the axial axis than along the radial axis. Moreover, in the partially polarized intermediate region, the order parameter has a small oscillation along the axial axis, but not along the radial axis. Similar order parameter oscillations were also found in the spherical trap case [39]. This is a consequence of the proximity effect which, in the context of superconductor, occurs when a superconductor is in contact with a normal metal, the Cooper pairs from the superconductor diffuse into the normal component.

Next, we increase the trap aspect ratio to $\alpha = 50$ which represents a much more elon-

gated cigar trap and close to what is used in the Rice experiment. A similar display of the column and axial spin density profiles for different polarization as in Fig. 2.3 is shown in Fig. 2.5. In this very elongated trap, the majority and minority components have their densities matched along the radial axis up to the highest polarization we have calculated which is $P = 0.7$, and the minority component has a boxy-looking density profile. This further confirms that the system is able to greatly reduce the effective surface area between the normal state and the superfluid state in anisotropic cigar-like traps. Another marked feature for such an elongated trap is the prominent oscillations of the order parameter along the z-axis. As demonstrated in Fig. 2.6, these oscillations are quite generic features in such a trap with finite P. As P increases, both the amplitude and the spatial extension of the oscillations increase. As shown in Fig. 2.6(b), at large polarizations, the axial length of the partially polarized intermediate region becomes comparable to or even larger than that of the BCS core. Accompanied by the oscillation in the order parameter, the density profiles (in particular, the minority density) also exhibit strong oscillations, which are reminiscent of the FFLO state.

Our calculations also show that these axial oscillations are aligned along the radial axis, as shown in Fig. 2.6(c). We even intentionally started from an initial ansatz of Δ where the axial oscillations are present but with the nodes mis-aligned in the radial direction, and the BdG iterations eventually converge to a state where the nodes are perfectly aligned radially. This radial alignment has important impact in detecting the oscillations in column density profiles where the densities are integrated along one radial axis: Due to the radial

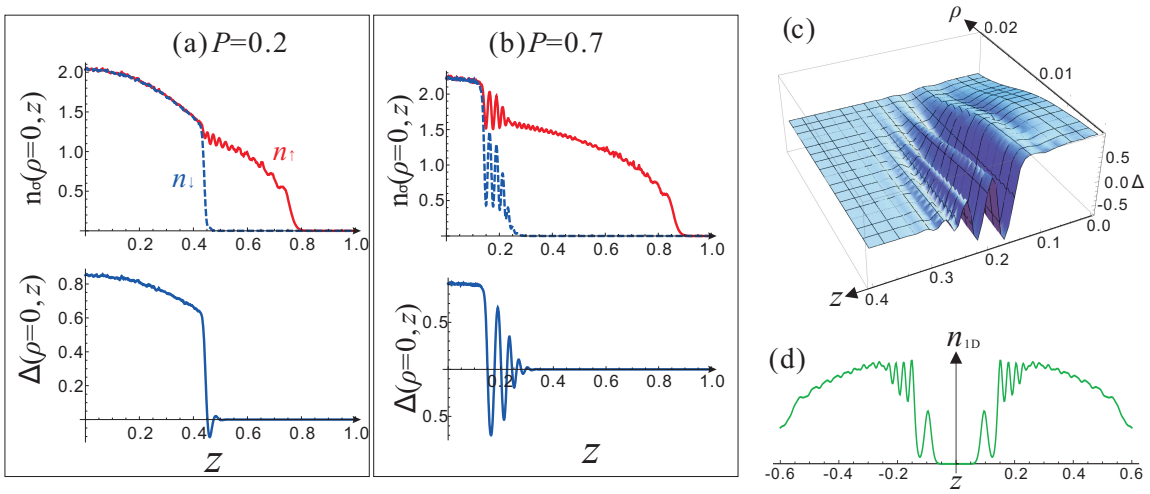

Figure 2.6: $\alpha = 50$ for two different polarizations: (a) $P = 0.2$ and (b) $P = 0.7$. Adopted from Ref. [27]. Same units as in Fig. 2.4. We do not show the radial density and order parameter profiles, which look more or less like those in Fig. 2.4(a). (c) The surface plot of the order parameter for the case of $P = 0.7$ in the ρ-z plane, showing strong oscillations with the nodes aligned along the radial direction. (d) The density oscillations for $P = 0.7$ leave a strong signal in the doubly integrated axial spin density $\delta\rho_{1D}(z)$.

alignment, the oscillations are not washed out and can be easily observed, for example, in the doubly integrated axial spin density $\delta\rho_{1d}(z)$, as illustrated in Fig. 2.6(d).

It is interesting to compare our result with the recent work by Bulgac et al. [59] who, using a density functional theory (DFT), argued that the FFLO pairing phase occupies a larger phase space region than people previously thought for a 3D homogeneous system. The FFLO state found in Ref. [59] is also associated with large-amplitude density oscillations, particularly in the minority component. Another perspective on the order parameter oscillations and its potential connection with the FFLO phase is dimensionality. It has been shown that the partially polarized phase with FFLO-like oscillations could be prominently featured in the phase space of 1D systems [60, 61, 62]. Besides the analogs of Fermi surface nesting, that FFLO state is favored in the reduced dimensionality can be understood alternatively from the cost of creating domain walls. The cigar-like traps used in our calculation mimic a quasi-1D system and may be the reason that we see pronounced oscillations in our calculation. If this latter explanation is correct, i.e., the partially polarized region featuring FFLO-like oscillations is due to the effective reduction of the spatial dimension, we then expect to see these oscillations diminish as N is increased while the trap aspect ratio is fixed, which makes the system more 3D-like. To check this, we keep $\alpha = 50$ but vary the total particle number N. Fig. 2.7 shows the density and order parameter along the axial and radial axis at a fixed polarization $P = 0.3$ but different values of total particle number N. As one can clearly see, the oscillations in both the order parameter and the density profiles diminish as N is increased and the LDA approximation becomes more and

more accurate, which indicates that the FFLO-like region observed above for small N does not represent a bulk 3D phase. Rather, it is a finite-size effect due to the effective reduction of the spatial dimension.

2.3.2 Linking to the experimental observation

Numerically, due to the high nonlinearity in BdG equation, with different initial ansatz, the solution may converge to distinct final states. While in the experiments, whether the ground state or a metastable state will be realized may depend upon how the evaporative cooling procedure is implemented [50]. This has been confirmed recently in a new experiment at Rice [51]. Thus, we take the approach of exploring the solution space using ansatze constructed with reference to [50] and the phase diagram on the BCS side of the Feshbach resonance [63, 64]. Specifically, we use the LDA solution for the gap (Δ_{LDA}) as a base to construct an initial ansatz Δ_I which is axially partitioned into different regions:

$$\Delta_I(r,z) = \begin{cases} \Delta_{\mathrm{LDA}} & |z| < z_c \\ \Delta_{\mathrm{LDA}} \cos[q(z-z_c)]\, e^{-(z-z_c)^2/\lambda^2} & |z| > z_c. \end{cases} \tag{2.26}$$

Δ_I allows us to explore various distorted states. In its most general form, one encounters the unpolarized BCS, FFLO, and normal phases as one traverses along the axial direction from the trap center to the edge. The initial size of the FFLO region in the ansatz is determined by λ. When λ is too small to accomodate a single wavelength of the gap oscillation, i.e., $0 < \lambda < 2\pi/q$, where $q = k_\uparrow - k_\downarrow$ is the anticipated FFLO oscillation wave number, we start without an FFLO phase and z_c represents the axial coordinate of superfluid

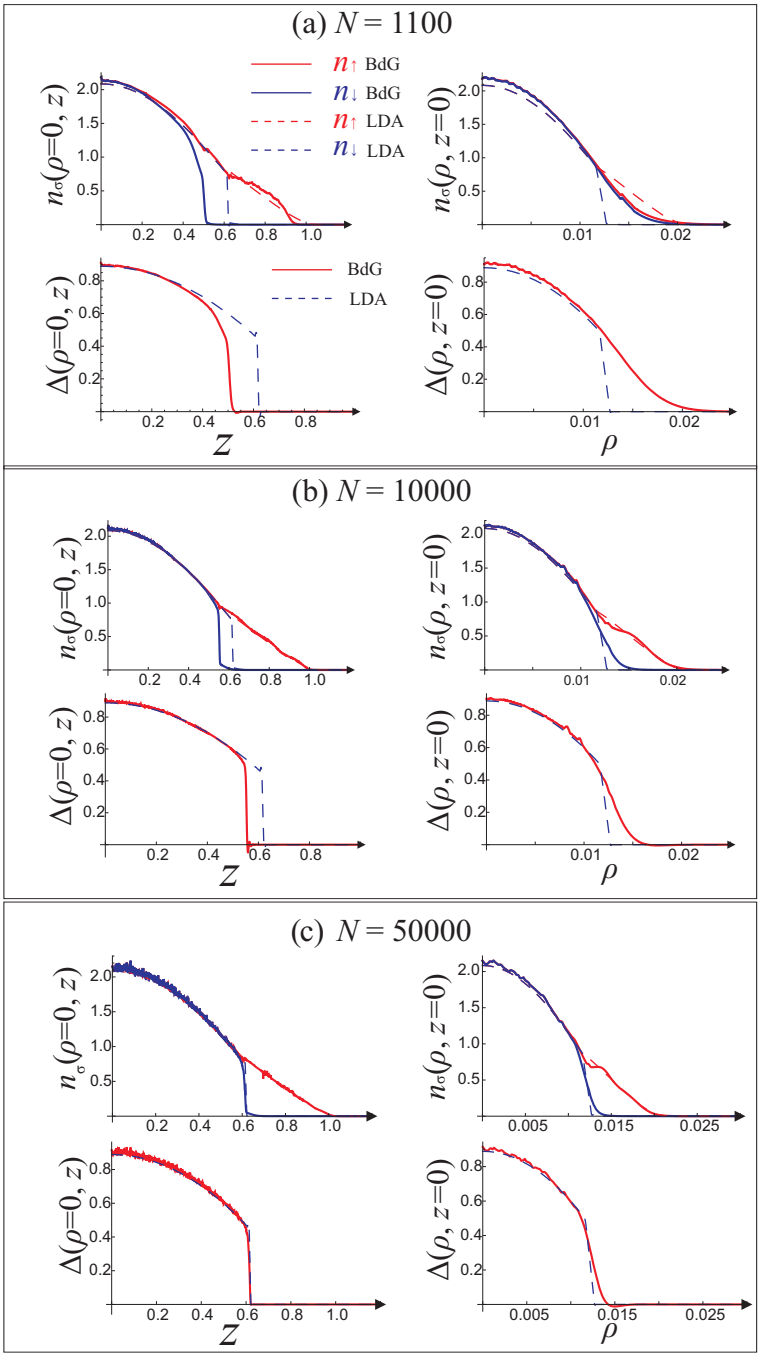

Figure 2.7: Density and order parameter profiles along the axial and the radial axis in a cigar-like trap with $\alpha = 50$ for $P = 0.3$ but different values of total particle number N. Adopted from Ref. [27]. Same units as in Fig. 2.4.

to normal (S/N) transition. Conversely, an FFLO phase is initially present in the ansatz when $\lambda > 2\pi/q$. In this case z_c represents the superfluid to FFLO (S/FFLO) transition. Henceforth we refer to these initial conditions as $\Delta_I^{\mathrm{P-N}}$ and $\Delta_I^{\mathrm{P-SF}}$, respectively, which reflects our nomenclature for the eventual solutions as well, i.e., we name the entire solution according to the character of the partially polarized region: We have a partially polarized superfluid solution (P-SF) when there is an FFLO-like phase present. When the partially polarized region is completely normal, we refer to the entire solution as a P-N solution. Here, for clarity we single out the LDA-like solution we have discussed in the previous section which is obtained when $\Delta_I = \Delta_{\mathrm{LDA}}$, as the SF solution. In both the P-N and P-SF solutions, the central unpolarized BCS superfluid core is shortened along the z-axis in comparison to the SF solution. As we shall see, this shortened BCS core is manifested in the LDA-violating distortion of the density profile of the the minority spin component.

A broad feature of our results, which directly informs on the question of metastability, is the observation of a barrier between the shortened states, either P-N or P-SF, and the SF solution. For small atom numbers, this barrier is absent, the converged solution is unique, independent of the initial ansatz we take, and we see a dramatic departure from the LDA prediction due to significant finite-size effect, which is demonstrated in section 2.3.1 for the study of $N = 200$ particles. However with increasing N, the axial S/N or S/FFLO transition point is pinned near its initial value z_c and we obtain different solutions by starting from different initial anstze. Starting from $\Delta_I^{\mathrm{P-SF}}$ or $\Delta_I^{\mathrm{P-N}}$ we always converge to a shortened state in a manner which is only sensitive to our choice of q. In other words, we do see a transition

between the P-SF and P-N states which is very sensitive to q and largely insensitive to λ; both of which are set in the initial condition Δ_I. It works as follows. When q is less than a critical value q_c, the oscillations in the ansatz Δ_I are amplified and the solution flows to a P-SF state oscillating with roughly the same q no matter the size of λ, and locally the FFLO oscillation wave number $q(z) = \sqrt{2(\mu_\uparrow - V_{\text{ext}}(z))} - \sqrt{2(\mu_\downarrow - V_{\text{ext}}(z))}$ is approximately uniform over the entire FFLO-like region as shown in the Fig. 2.8. Conversely when $q > q_c$, the oscillations are damped and Δ_I always converges to a P-N state. A similar resonance behavior has also recently been observed in studies of the S/N boundary while tuning a_s across the BEC-BCS crossover [44], in which case calculations were performed without the radial confinement.

We ascribe the consistent convergence to a shortened state as due to the emergence of energy barriers separating the P-SF and P-N states from the SF state with increasing N or α. In Fig. 2.8(a) we illustrate the dramatic differences in the superfluid gap for the various solutions encountered. Apart from the emerging energy barriers, another important result with regard to metastability is the decrease in the relative energetic separation of all the states, P-SF, P-N and SF, as α is increased. Taken together, these observations suggest that the relaxation of the physical system from any of the shortened states to the SF state, which is the lowest in energy, becomes less favorable as α is increased, a deduction which is borne out by the discrepancies of the Rice and MIT experiments.

For a given value of z_c, the energy of the P-SF solution is consistently lower than the P-N solution. Furthermore, the beyond mean-field DFT calculation by Bulgac et al. suggest

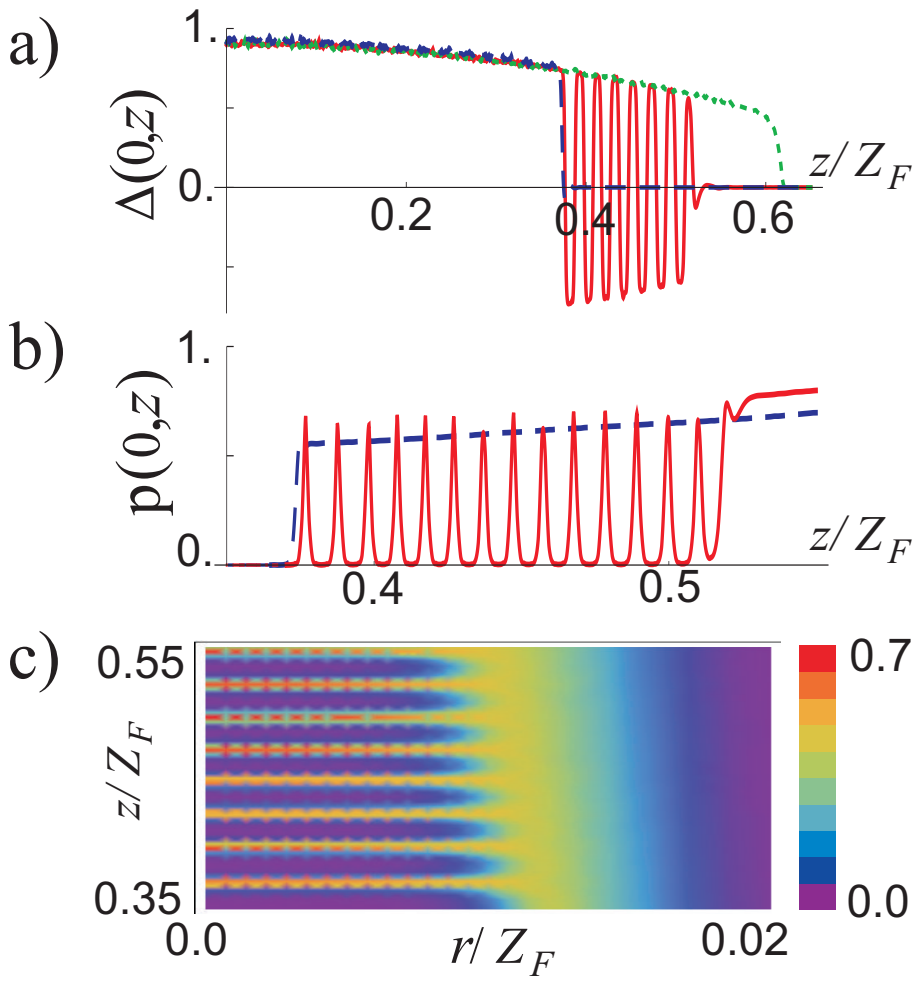

Figure 2.8: Adopted from Ref. [28]. (a) Axial profiles of the gap (in units of E_F) showing the P-N (blue dashed line), P-SF (red solid line) and SF (green dotted line) states. The LDA solution (not shown) almost completely overlaps with the SF result. The free energies per particle are: $0.67(0)E_F$, $0.65(8)E_F$, $0.65(5)E_F$ and $0.64(4)E_F$ for the P-N, P-SF, SF and LDA states, respectively. (b) Local polarization $p(\mathbf{R})$ within the partially polarized region of the P-SF(red solid line) and P-N(blue dashed line) solutions. (c) An r-z plot of the normalized density difference $\delta\rho = (\rho_\uparrow - \rho_\downarrow)/\rho_F$ of the partially polarized region of the P-SF state ($\rho_F = \sqrt{(2E_F)^3}/6\pi^2$). All the results shown in this paper are obtained at a small temperature $T = 0.02E_F/k_B$, and with $N = 50000$, $\alpha = 50$, and $P = 0.3$.

that the inclusion of fluctuations should make the P-SF state even more stable [59]. Thus, we expect that if the system converges to a shortened state, it will choose the P-SF state. Now let us have a closer look at the manifestations of FFLO state in the P-SF state.

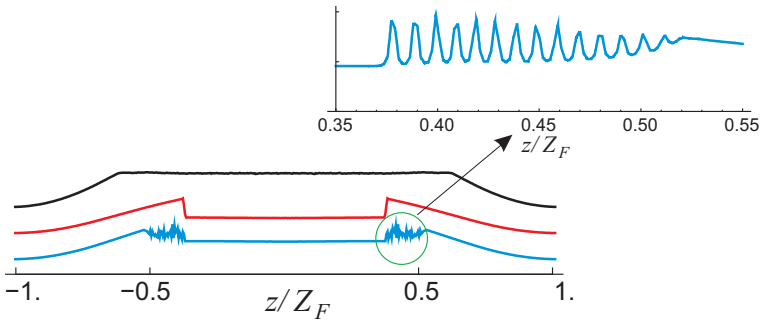

Figure 2.9: Plots showing the doubly integrated axial spin density $\delta\rho_{1d}(z)$ for, from top down, the SF, P-N and P-SF states shown in Fig. 2.8(a). Adopted from Ref. [28]

In Fig. 2.8(b) we contrast the appearance of local polarization $p(\mathbf{R}) = (\rho_\uparrow - \rho_\downarrow)/(\rho_\uparrow + \rho_\downarrow)$ in the partially polarized regions of the P-SF and P-N states. We note that in [59], the strong oscillations displayed in $p(\mathbf{R})$ were observed to survive the effects of fluctuations. We are pleased to observe that Fig. 2.8(c) still shows radial alignment of the nodes of the FFLO phase as in $N = 200$ case. Auspiciously, it also suggests that when an array of 1D tubes, such as the ones are being used in current experiments [26], are coupled to yield a quasi-3D confinement, the FFLO nodes at each tube are likely to align to yield a measurable signal. A comparison of the plots in Fig. 2.9 confirms that the presence of an FFLO phase would indeed provide a smoking gun signal in doubly integrated axial spin density $\delta\rho_{1d}$. In the close-up we observe that the signal of the FFLO region is not as strong as that in Fig. 2.8(c) because of contributions from the fully polarized shell encasing it.

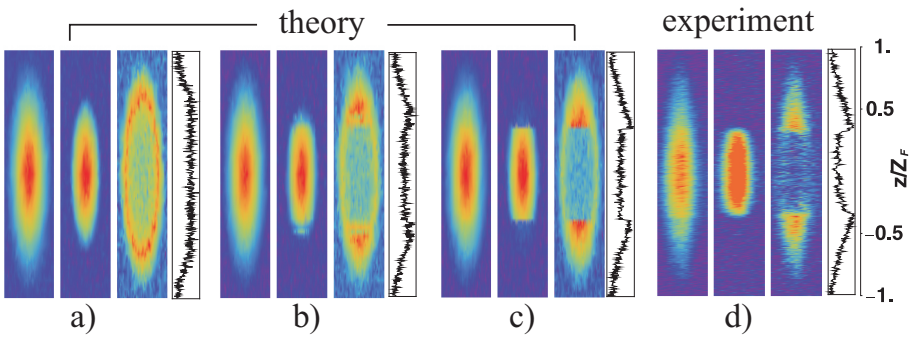

Figure 2.10: Each display shows the column densities (rescaled to have aspect ratio 5 for clarity) $\int \rho_\uparrow dx$, $\int \rho_\downarrow dx$, $\int (\rho_\uparrow - \rho_\downarrow) dx$ and the axial spin density $\delta\rho_{1d}$, respectively. The states represented are (a) the SF, (b) P-SF and (c) P-N states illustrated in Fig. 2.8(a). In (d) we plot the Rice experimental results for $N \approx 260000$, $P \approx 0.35$, $\alpha = 45.23$ and $T < 0.05 E_F/k_B$. Adopted from Ref. [28]

Quantitatively, it indicates that a lower bound of the signal to noise ratio ≈ 6.5 is required to observe at least half of the FFLO phase.

A casual comparison of all column density profiles in Fig. 2.10 rules out the observation in Rice experiment of the SF state, which is consistent with the LDA and, within the BdG formulation, has the lowest free energy. However, due to the noise on the experimental data, it is not clear which of the shortened states (P-SF or P-N) has been observed. To produce noise with similar characteristics as that in the experiment, we added white noise with standard deviation which is a similar fraction of the average value of the column density $\int_{-\infty}^{\infty} \rho_\uparrow \, dx$ in the plotted window. Theoretically, since it has the lower energy and since the transition between the FFLO phase and the normal phase is continuous, one expects that, between the two shortened states, the P-SF solution will be favored.

Chapter 3

Expansion of one-dimensional polarized ultracold Fermi gases

3.1 Introduction

In this chapter, we move our focus to the one-dimensional polarized Fermi gases, which, as previously discussed, would be much more promising in capturing the signals of the FFLO states. There has been copious theoretical evidence that FFLO correlations will occur and also be fairly robust in a polarized degenerate Fermi gas confined to a 1D harmonic trap [48, 60, 65, 66, 67, 68, 69, 70]. A dramatically different phase diagram [61, 72] from that in 3D is predicted for these 1D systems, and the recent Rice experiment [26] has confirmed the most important aspect of this phase diagram. The theory and experiment both show that the density profile of 1D polarized Fermi gases always exhibit a partially

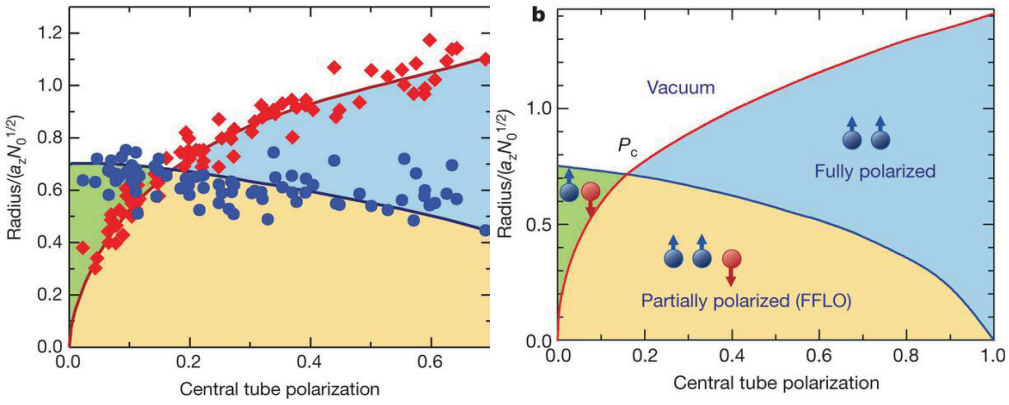

Figure 3.1: Polarized Fermi gases in one-dimension, right: The theoretically predicted phase diagram of 1D polarized Fermi gases. left: The experimental verification of the phase diagram showing perfect agreement to the theoretical calculation. The x axis represents the polarization in the central 1D tube left while the y axis represents the distance from the center of the tube. Figures are adopted from Ref. [26]

.

polarized core while the wings can be either fully polarized or fully paired as shown in Fig. 3.1 depending on the degree of imbalance.

Although a partially polarized phase was observed through direct imaging in the experiment, it is quite clear from recent work that the FFLO correlations *may not* leave a strong detectable signature on the ground state density profiles. Thus the character of the partially polarized phase remains unknown. Here we propose that such evidence is possible to be observed during a non-equilibrium expansion after the gas is suddenly released from the confinement. Our numerical experiment shows the polarized 1D Fermi gas develops strong signatures in the density profiles of the pairing species which are a direct consequence of

the FFLO crystalline order and constitute incontrovertible evidence for experiment observation.

We model the system as a gas of N fermionic particles each of mass m with two spin projections labeled by $\sigma = (\uparrow, \downarrow)$ initially confined to a cigar-shaped harmonic trap. In accordance with the experimental situations [26, 30, 31, 34, 40, 73], we assume that the inter-particle interaction arises from a broad Feshbach resonance and is thus highly controllable. In these systems, the ratio of the radial $\omega_\perp$ and axial ω_z trapping frequencies which defines the anisotropy of the trap, $\alpha = \omega_\perp/\omega_z$, can be made so large that the Fermi energy E_F associated with the axial dynamics of the trap $N\hbar\omega_z$ and the temperature k_BT, are both much smaller than the energy level spacing of the radial confinement $\hbar\omega_\perp$ i.e., $N\hbar\omega_z$, $k_BT << \hbar\omega_\perp$ [26]. Due to the extremely rarefied nature of the gas, the atomic physics at play and the one-dimensional nature of the confinement, there are virtually no spin relaxation processes and the particles interact via s-wave scattering $g_{1\mathrm{D}}\delta(z)$. The total polarization of the cloud $P = (N_\uparrow - N_\downarrow)/(N_\uparrow + N_\downarrow)$ is defined as previously. Formally, this system is described by the Hamiltonian $\hat{H} = \int dz\,(H_0 + H_I)$ with:

$$\begin{aligned} H_0(z) &= \sum_\sigma \psi_\sigma^\dagger \left[-\frac{\hbar^2}{2m}\frac{\partial^2}{\partial z^2} + V_{\mathrm{ext}}(z) - \mu_\sigma \right] \psi_\sigma \\ H_I(z) &= g_{1D}\psi_\uparrow^\dagger(z)\psi_\downarrow^\dagger(z)\psi_\downarrow(z)\psi_\uparrow(z) \end{aligned} \tag{3.1}$$

where $\psi_\sigma(z)$ and μ_σ are fermionic field operators and the chemical potential, respectively, of atomic species with spin σ, and $V_{\mathrm{ext}}(z) = \frac{m}{2}\omega_z^2 z^2$. We define the Fermi energy, radius, momentum and temperature as $E_F = N$, $Z_F = \sqrt{2E_F}$, $k_F = \sqrt{2E_F}$ and $T_F = E_F$. We measure the relative strength of the interaction with the ratio (γ) of the interaction (ϵ_I) and

the kinetic (ϵ_k) energy densities. In the limit of weak interaction $\epsilon_I \sim g_{1\mathrm{D}}\rho(z)$ and $\epsilon_k \sim \rho^2(z)$ yielding:

$$\gamma = g_{1\mathrm{D}}/\rho \tag{3.2}$$

The 1D effective coupling constant $g_{1D} < 0$ is expressed through a relation with the 3D scattering length a_{3D} by [74]: $g_{1D} = \frac{2\hbar^2 a_{3D}}{m a_l(1-Aa_{3D}/a_l)}$. Here a_l is the radial oscillator length and $A = \xi(1/2)/\sqrt{2} \approx 1.0326$, where the ξ is the Riemann Zeta function. As usual, we work in 'trap' units: $m = \omega_z = \hbar = k_B = 1$.

Our calculations are done using two methods with distinct but complementary advantages. First is the Time Evolving Block Decimation (TEBD) [75, 76], an unbiased approach that retains all important correlations. Second is the previously discussed mean-field BdG method, an effective-theory approach which describes the spin densities $\rho_\sigma(z)$ and the superfluid gap $\Delta(z)$ through quasi-particle wavefunctions. The BdG has the advantage that, when correct, it provides a clear picture of the dynamics of the pairing field $\Delta(z) = g_{1\mathrm{D}}\langle\psi_\uparrow(z)\psi_\downarrow(z)\rangle$ in direct association with the particle densities $\rho_\sigma(z) = \langle\psi^\dagger_\sigma(z)\,\psi_\sigma(z)\rangle$. However, although the BdG has been observed to give a very good description of 1D samples at weak interaction [60], we do not expect this trend to extend from moderate to strong interactions. Complementarily, the TEBD method provides a stringent check for the phenomena observed in the BdG approach. In both cases we work at $T = 0$ [77] and employ a canonical approach which fixes N and P.

3.2 Mean-Field treatment: time-dependent BdG formalism

In order to study the expansion dynamics, we first need solve the static BdG equation for the ground state of the trapped cold atom sample. Similar to what we have done in the previous chapter, we can still simply state the BdG equations for the pair wave functions $u_j(z)$ and $v_j(z)$ which decouple Hamiltonian $\hat{H}$:

$$\begin{bmatrix} H^s_\uparrow(z) - \mu_\uparrow & \Delta(z) \\ \Delta(z) & -H^s_\downarrow(z) + \mu_\downarrow \end{bmatrix} \begin{bmatrix} u_j(z) \\ v_j(z) \end{bmatrix} = E_j \begin{bmatrix} u_j(z) \\ v_j(z) \end{bmatrix}, \tag{3.3}$$

where

$$H^s_\sigma(z) = -\frac{1}{2}\frac{\partial^2}{\partial z^2} + V_{\text{ext}}(z)$$

and E_j is the associated energy. Similarly, the system is subject to normalization : $\int dz|u_j(z)|^2 + |v_j(z)|^2 = 1$. And the order parameter $\Delta(z)$ may be written as :

$$\Delta(\vec{r}) \;=\; g_{1D} \sum_{j=1}^{\infty} u_j(z) v_j^*(z) f(E_j) \tag{3.4}$$

where $f(E)$ represents the Fermi-Dirac distribution function: $f(E) = 1/(e^{E/k_BT} + 1)$. We follow a convention that $N_\uparrow > N_\downarrow$, and define $k_F^{\uparrow\downarrow} = \sqrt{2\mu_{\uparrow\downarrow}}$ and the FFLO wave number by $q_0 = k_F^\uparrow - k_F^\downarrow$. We can solve this BdG equation by following the procedure mentioned in Chapter 2. After obtaining the ground state, we remove the trapping confinement from the single particle Hamiltonian and employ Runge-Kutta scheme to propagate $u_j(z)$ and $v_j(z)$ using the time-dependent form of the BdG equation:

$$\begin{bmatrix} H_{\uparrow}^{E} - \mu_{\uparrow} & \Delta(z,t) \\ \Delta(z,t) & -H_{\downarrow}^{E} + \mu_{\downarrow} \end{bmatrix} \begin{bmatrix} u_j(z,t) \\ v_j(z,t) \end{bmatrix} = i\hbar \frac{\partial}{\partial t} \begin{bmatrix} u_j(z,t) \\ v_j(z,t) \end{bmatrix}, \tag{3.5}$$

where $H_{\sigma}^{s}(z)$ is replaced by $H_{\sigma}^{E}(z)$ as

$$H_{\sigma}^{E}(z) = -\frac{1}{2}\frac{\partial^2}{\partial z^2}$$

3.3 Numerics: Time-Evolving Block Decimation Algorithm

In this section, we provide an overview of the TEBD method, which is an alternative method we employed to investigate the expansion dynamics of 1D polarized Fermi gases.

3.3.1 Introduction

In the past couple of decade, for 1D quantum systems, one category of numerical technique, called density matrix renormalization group (DMRG), originally proposed by White in 1992 [78], has been successfully implemented on various well known models. While the DMRG is considered to be a numerically 'exact' method for solving static ground state properties of 1D models, it remains a challenging problem to apply this powerful scheme to study the dynamics. The solution came from quantum information physics, a newly developed branch of modern physics. One of the most important tasks of quantum information physics is to search for certain genuine quantum algorithms which are only suitable for a quantum computer as such algorithms will have extremely bad performance on a clas-

sical computer. In practice, the implementation of such algorithms is essentially beyond the capabilities of classical computers. It turns out that the failure of realizing a quantum algorithm on classical computers is due to a high degree of quantum entanglement [79] in the systems of interest. In 2003, Vidal [75] showed that, for 1D quantum systems with limited entanglement, there exists a time evolution algorithm, which is later referred to as TEBD algorithm and can be performed on a classical computer efficiently. From the perspective of practical implementation, TEBD algorithm can be easily adopted into well developed DMRG scheme, leading to an adaptive time-dependent DMRG [80]. With all these merits, TEBD makes itself a powerful tool for studying the time-dependent quantum many-body systems in 1D. In this sense, TEBD algorithm is the best fit for our purpose to study the expansion dynamics of 1D polarized Fermi gases. In this section, we briefly introduce the basic concepts and formalism of TBED method, as well as describe the practical procedure using the algorithm to simulate the 1D system and extract physical observables. The derivations we present here follow closely that given in Ref. [81], and our numerical implementation is based on the corresponding open source code.

3.3.2 Vidal decomposition

If a system contains N sites with local dimension of d, in general, a quantum state in such system can be expressed as

$$|\Psi\rangle = \sum_{i_1 \ldots i_N=1}^{d} c_{i_1 \ldots i_N} |i_1 \ldots i_N\rangle \tag{3.6}$$

We will thus have d^N coefficients $c_{i_1 \ldots i_N}$, which is the size of the Hilbert space. Due to this exponential dependence on N, it is easy to see that a simulation of such a system will become beyond classical computing capacity even for a very small N. In physics, an approximate solution can be achieved by introducing a variational ansatz which truncates the system's Hilbert space effectively while preserving the 'essential' physical properties we are interested in. One of the most widely adopted ansatz is the mean-field one, which simply restrict the a many-body quantum state to be a product state $|\Psi\rangle = \sum_{i_1 \ldots i_{N=1}}^{d} c_{i_1} \ldots c_{i_N} |i_1\rangle \ldots |i_N\rangle$, which reduces the size of the Hilbert space from $d^N$to dN. The mean-field ansatz neglects all quantum correlations and hence is over-simplified under many situations. For 1D many-body systems, in particular, it is highly unreliable because quantum fluctuations become more pronounced in lower dimensions. The TEBD method recasts the form of $|\Psi\rangle$ in Eq. (3.6) into a tensor product form. The corresponding N-body coefficient $c_{i_1 \ldots i_N}$ can be expressed in a form called Vidal's decomposition, which is a sum over product of local vector $\lambda^{[l]}$ and local tensor $\Gamma^{[l]}$:

$$c_{i_1 \ldots i_N} = \sum_{\alpha_1 \ldots \alpha_L}^{\chi} \Gamma^{[1]i_1}_{\alpha_1} \lambda^{[2]}_{\alpha_1} \Gamma^{[2]i_2}_{\alpha_1 \alpha_2} \lambda^{[3]}_{\alpha_2} \Gamma^{[3]i_3}_{\alpha_2 \alpha_3} \ldots \Gamma^{[L]i_L}_{\alpha_{L-1}} \tag{3.7}$$

here we restrict our discussion to an open boundary condition which we use for our calculation and χ is the Schmidt rank associated with the bipartite splitting procedure. Now with this form, the total number of coefficients we have, i.e., λ's and Γ's, has been reduced to $dN\chi^2 + (N+1)\chi$. If χ scales polynomially in system size, the Vidal decomposition can help us achieve an exponential speedup.

To see the validity of TEBD, we can start from an arbitrary bipartition of the system

into two subsets, say, A and B. By using the well-known Schmidt decomposition, we can write the state as following:

$$|\Psi\rangle = \sum_{\alpha=1}^{\chi_A} \lambda_\alpha \left|\Phi_\alpha^A\right\rangle \otimes \left|\Phi_\alpha^B\right\rangle = \sum_{\alpha_l=1}^{\chi_A} \lambda_{\alpha_l}^{[l+1]} \left|\Phi_{\alpha_l}^{[1\ldots l]}\right\rangle \otimes \left|\Phi_{\alpha_l}^{[l+1\ldots N]}\right\rangle \tag{3.8}$$

where $\lambda_{\alpha_l}^{[l+1]}$ is the Schmidt coefficients which satisfy $\sum_{\alpha_l=1}^{\chi_A} (\lambda_{\alpha_l}^{[l+1]})^2 = 1$. $\left|\Phi_\alpha^{[1\ldots l]}\right\rangle$ and $\left|\Phi_\alpha^{[l+1\ldots N]}\right\rangle$ are, respectively, the eigenvalues of the reduced density matrices $\rho^{[1\ldots l]} = \mathrm{Tr}_{(l+1)\ldots N} |\psi\rangle\langle\psi|$ and $\rho^{[l+1\ldots N]} = \mathrm{Tr}_{1\ldots l} |\psi\rangle\langle\psi|$, $(\lambda_{\alpha_l}^{[l+1]})^2$ is the corresponding eigenvalue. χ_A is the Schmidt rank which satisfies $1 \leqq \chi_A \leqq \min(d^l, d^{N-l})$. We can carry out this procedure iteratively and finally obtain the decomposition of the state coefficients in the form as shown in Eq. (3.7). Now let us look into where the numerical errors are introduced in Vidal decomposition. Since there would be no approximation if we choose $\chi = \chi_A$, the numerical error is incurred when we choose to keep only $\chi < \chi_A$ largest eigenvalues $\lambda_{\alpha_l}^{[l+1]}$. We can introduce the so-called Schmidt measure $E_\chi = \log\chi$ to evaluate how this approximation preserves the entanglement in the many-body system. Optimally, if the 1D quantum system is critical and finite-range interacting, it can be proven that the von Neumann entropy will scale as $S \sim \log N$ [82]. Therefore we may conclude that the cutoff parameter χ scales polynomially in the system size as desired and the Vidal decomposition can be used to faithfully represent the quantum states in such systems.

3.3.3 Operations in the Vidal representation

Up to now, we haven't seen the power of Vidal decomposition. To find out this, we need to inspect how unitary operations act in Vidal representation. Most Hamiltonians in 1D

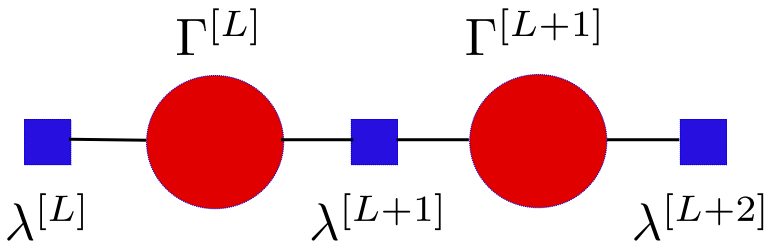

Figure 3.2: The tensor structure of the Vidal decompostion

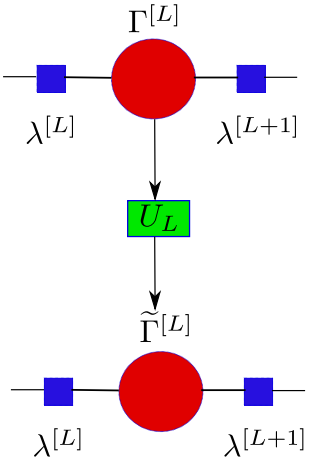

Figure 3.3: One-Site operation in the Vidal representation

only involve single-site and two-site operations on wavefunctions. Therefore, based on this observation, it is convenient for us to only consider these two categories of operators. First consider applying an unitary operator $\hat{U}$ which acts on lth single site:

$$\hat{U} = \sum_{i_l, i'_l} U_{i_l i'_l} |i_l\rangle \langle i'_l| \tag{3.9}$$

As shown in Fig. 3.3, this operation will not affect the left Schmidt coefficient when we perform Schmidt decomposition at link l, therefore $\Gamma^{[i]}$ and $\lambda^{[i+1]}$ for $i \leq l-1$ will be left untouched. Similarly we can see that $\Gamma^{[i]}$ and $\lambda^{[i]}$ for $i \geq l+1$ will keep unchanged. So we

can conclude that the only affected local tensor is $\Gamma^{[l]}$ and the transformation has the form as follows:

$$\widetilde{\Gamma}^{[l]i_l}_{\alpha_{l-1}\alpha_l} = \sum_{i'_l} U_{i_l i'_l} \Gamma^{[l]i'_l}_{\alpha_{l-1}\alpha_l} \tag{3.10}$$

Next we consider a two-site operation $\hat{V}$ which acts on two neighboring sites l and $l+1$ as shown in Fig. 3.4 :

$$\hat{V} = \sum_{i_l, i_{l+1}, i'_l, i'_{l+1}} V^{i_l i_{l+1}}_{i'_l i'_{l+1}} \left| i_l i_{l+1} \right\rangle \left\langle i'_l i'_{l+1} \right| \tag{3.11}$$

We put the initial state into a form of bipartite splitting between l and $l+1$

$$|\Psi\rangle = \sum_{\alpha_{l-1}\alpha_l\alpha_{l+1}; i_l, i_{l+1}} \lambda^{[l]}_{\alpha_{l-1}} \Gamma^{[l]i_l}_{\alpha_{l-1}\alpha_l} \lambda^{[l+1]}_{\alpha_l} \Gamma^{[l+1]i_{l+1}}_{\alpha_l\alpha_{l+1}} \lambda^{[l+2]}_{\alpha_{l+1}} \left| \Phi^{[1\ldots l-1]}_{\alpha_{l-1}} \right\rangle \otimes |i_l i_{l+1}\rangle \otimes \left| \Phi^{[l+2\ldots N]}_{\alpha_{l+1}} \right\rangle \tag{3.12}$$

then we can introduce an object Θ

$$\Theta^{i_l i_{l+1}}_{\alpha_{l-1}\alpha_{l+1}} = \sum_{\alpha_l} \lambda^{[l]}_{\alpha_{l-1}} \Gamma^{[l]i_l}_{\alpha_{l-1}\alpha_l} \lambda^{[l+1]}_{\alpha_l} \Gamma^{[l+1]i_{l+1}}_{\alpha_l\alpha_{l+1}} \lambda^{[l+2]}_{\alpha_{l+1}} \tag{3.13}$$

then rewrite the expression of $|\Psi\rangle$ as

$$|\Psi\rangle = \sum_{\alpha_{l-1}\alpha_{l+1}; i_l, i_{l+1}} \Theta^{i_l i_{l+1}}_{\alpha_{l-1}\alpha_{l+1}} \left| \Phi^{[1\ldots l-1]}_{\alpha_{l-1}} \right\rangle \otimes |i_l i_{l+1}\rangle \otimes \left| \Phi^{[l+2\ldots N]}_{\alpha_{l+1}} \right\rangle \tag{3.14}$$

with this transformation, after applying the two-site operation $\hat{V}$, only Θ needs to be updated as

$$\widetilde{\Theta}^{i_l i_{l+1}}_{\alpha_{l-1}\alpha_{l+1}} = \sum_{i'_l i'_{l+1}} V^{i_l i_{l+1}}_{i'_l i'_{l+1}} \Theta^{i'_l i'_{l+1}}_{\alpha_{l-1}\alpha_{l+1}} = \lambda^{[l]}_{\alpha_{l-1}} \widetilde{\Gamma}^{[l]i_l}_{\alpha_{l-1}\alpha_l} \widetilde{\lambda}^{[l+1]}_{\alpha_l} \widetilde{\Gamma}^{[l+1]i_{l+1}}_{\alpha_l\alpha_{l+1}} \lambda^{[l+2]}_{\alpha_{l+1}} \tag{3.15}$$

and we arrive at that

$$|\Psi\rangle = \sum_{\alpha_{l-1}\alpha_{l+1}; i_l, i_{l+1}} \widetilde{\Theta}^{i_l i_{l+1}}_{\alpha_{l-1}\alpha_{l+1}} \left| \Phi^{[1\ldots l-1]}_{\alpha_{l-1}} \right\rangle \otimes |i_l i_{l+1}\rangle \otimes \left| \Phi^{[l+2\ldots N]}_{\alpha_{l+1}} \right\rangle \tag{3.16}$$

A practical algorithmical implementation follows such a procedure [81]: we first perform

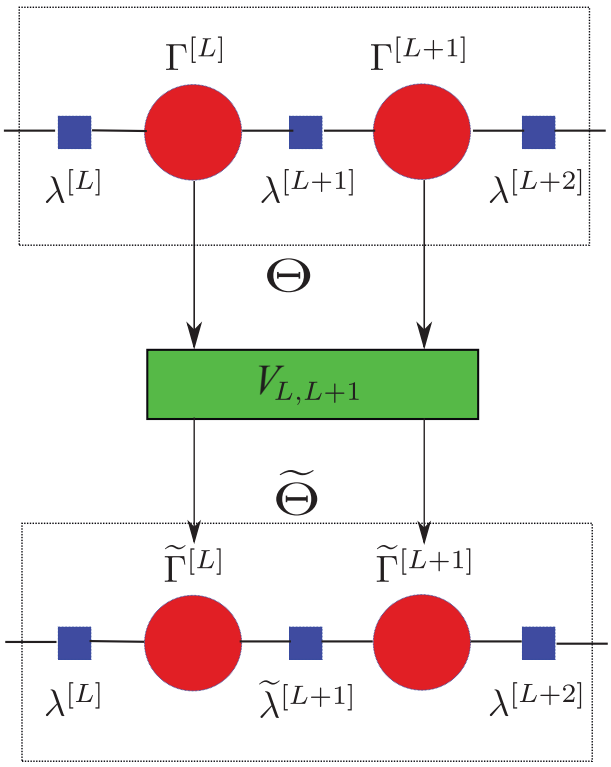

Figure 3.4: Two-Site operation in the Vidal representation

normalization $\sum_{\alpha,i,j,\gamma} \left|\widetilde{\Theta}^{ij}_{\alpha\gamma}\right|^2 = 1$ and recast the normalized $\widetilde{\Theta}$ into a $(\chi d) \times (\chi d)$ matrix $\widetilde{\Theta}_{RS}$, then a single value truncation will be preformed on $\widetilde{\Theta}_{RS}$ in which only the χ largest singular values are kept, finally we can update tensors $\widetilde{\lambda}^{[l+1]}_{\alpha_l}, \widetilde{\Gamma}^{[l]}, \widetilde{\Gamma}^{[l+1]}$ as follows

$$\widetilde{\Theta}_{RS} \xrightarrow{SVD} USV \tag{3.17}$$

$$\widetilde{\Gamma}^{[l]i_l}_{\alpha_{l-1}\alpha_l} = U_{(i_l-1)\chi+\alpha_{l-1},\alpha_l} / \lambda^{[l]}_{\alpha_{l-1}} \tag{3.18}$$

$$\widetilde{\Gamma}^{[l+1]i_{l+1}}_{\alpha_l\alpha_{l+1}} = V_{\alpha_l,(i_{l+1}-1)\chi+\alpha_{l+1}} / \lambda^{[l+2]}_{\alpha_{l+1}} \tag{3.19}$$

$$\widetilde{\lambda}^{[l+1]}_{\alpha_l} = S_{\alpha_l} / \sqrt{\sum_{\alpha=1}^{\chi} S^2_{\alpha}} \tag{3.20}$$

3.3.4 Trotter expansion

Now we show how to evolve a quantum state $|\Psi\rangle$ in the Vidal representation under a certain Hamiltonian $\hat{H}$. The unitary evolution operator thus is $\hat{U}(\delta t) = e^{(-i\hat{H}\delta t/\hbar)}$, where δt is the time interval. Generally such evolution operator is of a size of $d^N \times d^N$ even if only local interaction is involved. Therefore, for given many-body Hamiltonian $\hat{H}$, we need to find a way to decompose this time evolution operator into a series of one-site or two-site unitary operations so that we can put the method we discussed above into application. Fortunately as we have pointed out, a lot of well-known model Hamiltonians in 1D only consist of one-site operation or two-site operation acting on nearest neighbors. So we can decompose $\hat{H}$ as

$$\hat{H} = \sum_l \hat{H}_l = \sum_{\text{odd}} \hat{H}_l + \sum_{\text{even}} \hat{H}_l = \hat{H}_{\text{odd}} + \hat{H}_{\text{even}} \tag{3.21}$$

here the l is the index of a link, which means $\hat{H}_l$ acts on sites connecting to link l, i.e., site l and $l+1$. The reason that we divide $\hat{H}_l$ into odd and even subgroups is that $\hat{H}_l$ and $\hat{H}_{l+1}$ usually do not commute, which makes us unable to decompose the $\hat{U}(\delta t)$ into direct product of $e^{(-i\hat{H}_l\delta t/\hbar)}$. However, the terms in the subgroup H_{odd} or H_{even} will commute with each other since $\left[H_l, H_{l+j}\right] = 0, j \geqq 2$. Now the last step we need to do is to separate H_{odd} or H_{even} in the exponential and the natural way to proceed is to employ the well-known Suzuki-Trotter expansion, which was originally developed for quantum Monte Carlo method [83]. According to the first order Suzuki-Trotter expansion,

$$e^{\delta A+\delta B} = \lim_{\delta\to 0}(e^{\delta A}e^{\delta B} + O(\delta^2)) \tag{3.22}$$

and the accuracy can be improved to $O(\delta t^3)$ by taking a symmetric form to obtain the second order expansion

$$e^{\delta A+\delta B} = \lim_{\delta\to 0}(e^{\delta A/2}e^{\delta B}e^{\delta A/2} + O(\delta t^3)) \tag{3.23}$$

Therefore, in our case, we can write

$$e^{-i\hat{H}\delta t/\hbar} = e^{-i\hat{H}_{\text{odd}}\delta t/2\hbar}e^{-i\hat{H}_{\text{even}}\delta t/\hbar}e^{-i\hat{H}_{\text{odd}}\delta t/2\hbar} + O(\delta t^3) \tag{3.24}$$

Since all terms within H_{odd} or H_{even} commute each other, we have

$$e^{-i\hat{H}_{\text{odd}}\delta t/2\hbar} = \prod e^{-i\hat{H}_l\delta t/2\hbar} \tag{3.25}$$

$$e^{-i\hat{H}_{\text{even}}\delta t/\hbar} = \prod e^{-i\hat{H}_l\delta t/\hbar} \tag{3.26}$$

Furthermore, there are various higher order perturbative expansion formalisms available. For the open boundary condition which we employed for our calculation, a fifth-order Suzuki-Trotter expansion is given by the Forest-Ruth formula as follows

$$\begin{aligned} e^{-i\hat{H}\delta t/\hbar} \quad = \quad & e^{-i\hat{H}_{\text{odd}}\theta\delta t/2\hbar}e^{-i\hat{H}_{\text{even}}\theta\delta t/\hbar}e^{-i\hat{H}_{\text{odd}}(1-\theta)\delta t/2\hbar}e^{-i\hat{H}_{\text{even}}(1-2\theta)\delta t/\hbar} \\ & e^{-i\hat{H}_{\text{odd}}(1-\theta)\delta t/2\hbar}e^{-i\hat{H}_{\text{even}}\theta\delta t/\hbar}e^{-i\hat{H}_{\text{odd}}\theta\delta t/2\hbar} + O(\delta t^5) \end{aligned} \tag{3.27}$$

where $\theta = 1/(2 - 2^{1/3})$ is the Forest-Ruth parameter. With the higher-order expansion, we can use coarser time step $\delta t' = (\delta t)^{3/5}$ to reduce the effective computational time while achieving the same or even better accuracy.

The procedure discussed above can not only be used for real time propagation, but also works for seeking faithful ground state by using imaginary time evolution as usual, i.e., let $\tau \to it$ and evolve the state with the operator $\hat{U}(\delta\tau) = e^{(-\hat{H}\delta\tau/\hbar)}$. However, this is no

longer an unitary operation, therefore after each time step a renormalization of the state is required. Finally the obtained converged ground state can be expressed as

$$\left|\Psi_g\right\rangle = \lim_{\tau\to\infty} \frac{e^{(-\hat{H}\tau/\hbar)}\left|\Psi_0\right\rangle}{\left\|e^{(-\hat{H}\tau/\hbar)}\left|\Psi_0\right\rangle\right\|} \tag{3.28}$$

3.3.5 Calculation of observables

In order to faithfully represent a many-body system, a numerical algorithm should be capable to calculate all the relevant physical observables. In TEBD method, a majority of observables are calculated through the reduced density matrices which can be conveniently obtained from λs and Γs in the Vidal representation. Therefore we first show how to obtain the single-site and two-site reduced density matrices, $\hat{\rho}_l$ and $\hat{\rho}_{kl}$.

For the density matrix $\hat{\rho}$ of the full system, by tracing over all sites but l, we obtain

$$\hat{\rho}_l = \mathrm{Tr}_{k\neq l}(\left|\Psi\right\rangle\left\langle\Psi\right|) = \sum_{i_l,i_l'}\Big(\sum_{i_1\ldots i_{l-1},i_{l+1},\ldots i_N} c^*_{i_1\ldots i_l'\ldots i_N} c_{i_1\ldots i_l\ldots i_N}\Big)\left|i_l\right\rangle\left\langle i_l'\right| \tag{3.29}$$

To express this in terms of λ's and Γ's, we isolate the single site l

$$\left|\Psi\right\rangle = \sum_{i_l,\alpha_{l-1}\alpha_l}\left|\Phi^{[1\ldots l-1]}_{\alpha_{k-1}}\right\rangle \otimes \lambda^{[l]}_{\alpha_{l-1}}\Gamma^{[l]i_l}_{\alpha_{l-1}\alpha_l}\lambda^{[l+1]}_{\alpha_l}\left|i_l\right\rangle \otimes \left|\Phi^{[l+1\ldots N]}_{\alpha_l}\right\rangle \tag{3.30}$$

then tracing over all sites but l, we obtain that

$$(\hat{\rho}_l)_{i_l i_l'} = \sum_{\alpha_{l-1}\alpha_l}\lambda^{[l]}_{\alpha_{l-1}}(\Gamma^{[l]i_l'}_{\alpha_{l-1}\alpha_l})^*\lambda^{[l+1]}_{\alpha_l}\lambda^{[l]}_{\alpha_{l-1}}\Gamma^{[l]i_l}_{\alpha_{l-1}\alpha_l}\lambda^{[l+1]}_{\alpha_l} \tag{3.31}$$

Following the similar procedure, we can obtain two-site reduced density matrices $\hat{\rho}_{kl}$ by tracing over all sites but k and l. We skip the detailed derivation and jump to the final

results in terms of λs and Γs, assuming $k < l$

$$
\begin{aligned}
(\hat{\rho}_{lk})_{i_l i_k i'_l i'_k} = & \sum_{i_{k+1}\ldots i_{l-1}} \sum_{\alpha_{k-1},\alpha_l} \sum_{\alpha_k \ldots \alpha_{l-1}} \sum_{\alpha'_k \ldots \alpha'_{l-1}} \\
& (\lambda^{[k-1]}_{\alpha_{k-1}} \Gamma^{[k]i_k}_{\alpha_{k-1}\alpha_k} \lambda^{[k]}_{\alpha_k} \Gamma^{[k+1]i_{k+1}}_{\alpha_k\alpha_{k+1}} \lambda^{[k+1]}_{\alpha_{k+1}} \ldots \lambda^{[l-2]}_{\alpha_{l-2}} \Gamma^{[l-1]i_{l-1}}_{\alpha_{l-2}\alpha_{l-1}} \lambda^{[l-1]}_{\alpha_{l-1}} \Gamma^{[l]i_l}_{\alpha_{l-1}\alpha_l} \lambda^{[l]}_{\alpha_l}) \times \\
& (\lambda^{[k-1]}_{\alpha_{k-1}} (\Gamma^{[k]i'_k}_{\alpha_{k-1}\alpha'_k})^* \lambda^{[k]}_{\alpha'_k} (\Gamma^{[k+1]i'_{k+1}}_{\alpha'_k\alpha'_{k+1}})^* \lambda^{[k+1]}_{\alpha'_{k+1}} \ldots \lambda^{[l-2]}_{\alpha'_{l-2}} (\Gamma^{[l-1]i'_{l-1}}_{\alpha'_{l-2}\alpha'_{l-1}})^* \\
& \lambda^{[l-1]}_{\alpha'_{l-1}} (\Gamma^{[l]i'_l}_{\alpha'_{l-1}\alpha'_l})^* \lambda^{[l]}_{\alpha'_l})
\end{aligned} \tag{3.32}
$$

Using the reduced density matrices, we can calculate the expectation values of single-site or two-site observables as

$$\left\langle \hat{A}_l \right\rangle = \mathrm{Tr}(\hat{\rho}_l \hat{A}) \tag{3.33}$$

$$\left\langle \hat{B}_{kl} \right\rangle = \mathrm{Tr}(\hat{\rho}_{kl} \hat{B}) \tag{3.34}$$

In practical simulations, those observables could be density and pair correlation functions as we will discuss in the following section. The extension to the expectation of N-site observables is straightforward and the detailed method can be found in Ref. [84].

3.4 Expansion dynamics of polarized Fermi gases in 1D

With the mean-field BdG and TEBD methods discussed above, we are now able to start our comparative study of the real-time expansion dynamics of 1D polarized Fermi gases. However, to adopt the TEBD formalism for our purpose, we first need to derive the discrete model describing the system. We utilize the approach proposed by Tezuka et. al, to build a discrete Hamiltonian which can be used to represent a continuum system trustfully as shown in their DMRG simulation [68, 85].

3.4.1 Discretizing continuous system

Following the approach in Ref. [85], here again we only consider two-body s-wave interaction, we start with an effective Hamiltonian for continuum 1D polarized Fermi gases in harmonic traps, which has the form as follows:

$$\hat{H}_{\text{cont}} = \int dz \sum_{\sigma} \Psi_{\sigma}^{\dagger} \left(-\frac{\hbar^2}{2m} \frac{d^2}{dz^2} + V_{\text{ext}} \right) \Psi_{\sigma} + g_{1D} \int dz \, \Psi_{\uparrow}^{\dagger} \Psi_{\downarrow}^{\dagger} \Psi_{\downarrow} \Psi_{\uparrow} \tag{3.35}$$

where $V_{\text{ext}} = \omega_z^2 z^2/2$ is the trapping potential. From now on we take the trap units letting $\hbar = m = \omega_z = 1$. The above continnum Hamiltonian can be discretized over a 1D lattice by substituting the field operator

$$\Psi_{i,\sigma} \rightarrow c_{i,\sigma} / \sqrt{\Delta z} \tag{3.36}$$

and approximating the kinetic term

$$\frac{d^2}{dz^2} \Psi_{i,\sigma} \rightarrow (\Psi_{i+1,\sigma} + \Psi_{i-1,\sigma} - 2\Psi_{i,\sigma})/(\Delta z)^2 \tag{3.37}$$

where the subscript i denotes the ith site on the lattice, Δz is the lattice grid size, and $\Psi_{i,\sigma}, c_{i,\sigma}$ is the field operator and fermionic annihilation operator at the ith lattice site respectively. Discretizing the above continnum Hamiltonian on a 1D lattice with L sites, we can obtain a Fermi-Hubbard-like Hamiltonian as follows:

$$H = -J \sum_{\sigma} \sum_{i=2}^{L} (c_{i,\sigma}^{\dagger} c_{i-1,\sigma} + h.c.) + U \sum_{i=1}^{L} n_{i,\uparrow} n_{i,\downarrow} + \sum_{i=1}^{L} V_i (n_{i,\uparrow} + n_{i,\downarrow}) \tag{3.38}$$

where $c_{i,\sigma}^{\dagger}$, $c_{i,\sigma}$ is the fermionic creation and annihilation operator for spin-σ particles at ith lattice site, J is the hopping amplitude between the neighboring sites, and U is the on-site interaction strength between two spin species. To compare with the mean-field

BdG results, we need express the model parameters J and L in terms of system physical parameters. If we adopt the trap units used in BdG calculation, we have hopping amplitude $J = \frac{L^2}{2l^2}$, where l is the length of the 1D system, and thus parameters $\frac{U}{J} = 2g_{1D}(\frac{l}{L})$, $\frac{V_i}{J} = (\frac{l}{L})^4(i - \frac{L}{2})^2$ are choosen accordingly. In our simulation, we typically choose L to be $300 \sim 400$. The convergence of a TEBD calculation is mainly controlled by the parameter χ, which is the number of eigenvalues retained when truncating the Hilbert space. In practice, the computation time scales as the order of χ^3. Optimally we choose $\chi \sim 150$ to ensure the convergence is good enough when comparing with the results with higher χ. On the other hand, to reduce the intrinsic errors of TEBD resulted from the Trotter-Suzuki expansion for the time evolution operator, we adopt fifth-order Trotter-Suzuki expansion in our calculations with open boundary condition. The time step is optimally chosen to balance the accurancy and efficiency based on the self-consistent stability test.

As a benchmark study, we study a very weakly interacting Fermi gas in which $g_{1D} = -1.4$ and polarization $P = 0.05$. It is expected that BdG method can generate reliable results in this case, which thus can be used as a bechmarking check for TEBD result using the discretized model. We use both method to calculate the ground state, and comparison between the results from two methods is presented in Fig. 3.5. The density profile of ground state generated by two methods show perfect match at this interaction strength, confirming the validality of the discretized model.

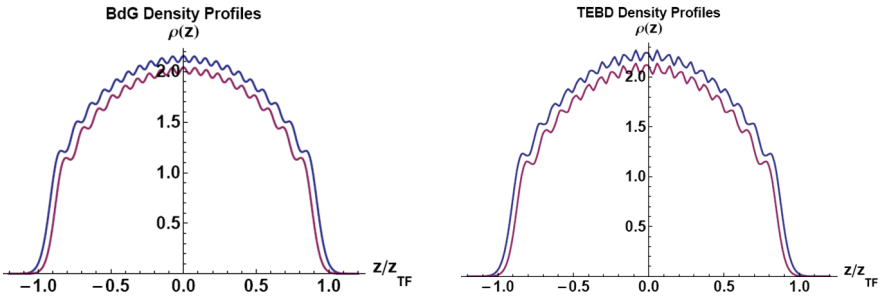

Figure 3.5: Comparing ground states obtained by BdG and TEBD when $g_{1D} = -1.4$ and $P = 0.05$.

3.4.2 Density modulations in expanding polarized gases

We now present the major discovery in our numerical studies. To observe the FFLO state, experiments must verify crystalline order in $\Delta(z)$ or, alternatively, that the average center-of-mass momentum of the pairs $\langle n_k \rangle$ is proportional to the separation of the Fermi surfaces, i.e., $\langle n_k \rangle \propto k_\uparrow - k_\downarrow$. Recently, a number of authors [66, 67, 86] have suggested that the time-of flight measurement of the pair-momentum distribution function n_k as the most promising avenue for detecting the finite center-of-mass momentum q of the pairs. These suggestions are extrapolations from equilibrium studies where n_k shows peaks at $k = \pm q$ in contrast to the peak at $k = 0$ expected for regular BCS pairing. However, we are not aware of analyses of the evolution of n_k accounting for the interacting nature of the expansion dynamics and in particular how well this signal will be preserved. This is particularly important for 1D given that γ increases during expansion [see Eq. (3.2)]. In our study we explore the possibility of finding a signal directly in real space. Our calculations reveal that: (1) Upon

axial expansion, strong peaks develop in the spin density profiles. (2) The position of these peaks exactly coincide with the nodes in the pair correlation function and represent *prima facie* evidence of FFLO correlations. (3) The strength of this signal increases with γ and decreases with polarization, being strongest when the spin excitations are gapped. (4) The peaks in the spin density move much more slowly than the edge of the cloud.

In Fig. 3.6 dramatic modulation in the spin densities are observed as the cloud expands. Through a comparison of the density plots with the corresponding gap parameter $|\Delta(z)|$ (the bottom row in Fig. 3.6) one can make a key observation: *The position and growth of the spin density peaks respectively coincide with the nodes and amplification of* $|\Delta(z)|$. Furthermore, these spin density peaks (or the order parameter nodes) move much slower during the expansion as compared to the edge of the whole cloud as shown in Fig. 3.7. We note that this is not a manifestation of the spin-charge separation as here the spin refers not to an excitation in the spin sector, but rather excess majority atoms. In fact, previous studies have indicated that, in a spin-imbalanced system, the spin and charge excitations are coupled [87, 88, 89].

To understand this phenomenon, it is helpful to first layout some broad features of the ground state utilizing the phase diagram for a homogeneous system together with the LDA treatment [61, 68, 72, 85]. There are two regimes to be considered [26, 60, 62, 65, 66, 68] depending on whether P is smaller or larger than a critical polarization P_c, which is approximately 0.1 at this interaction strength according to our simulation. For $P < P_c$, we obtain an FFLO state at the center of the trap surrounded by fully paired BCS wings at the

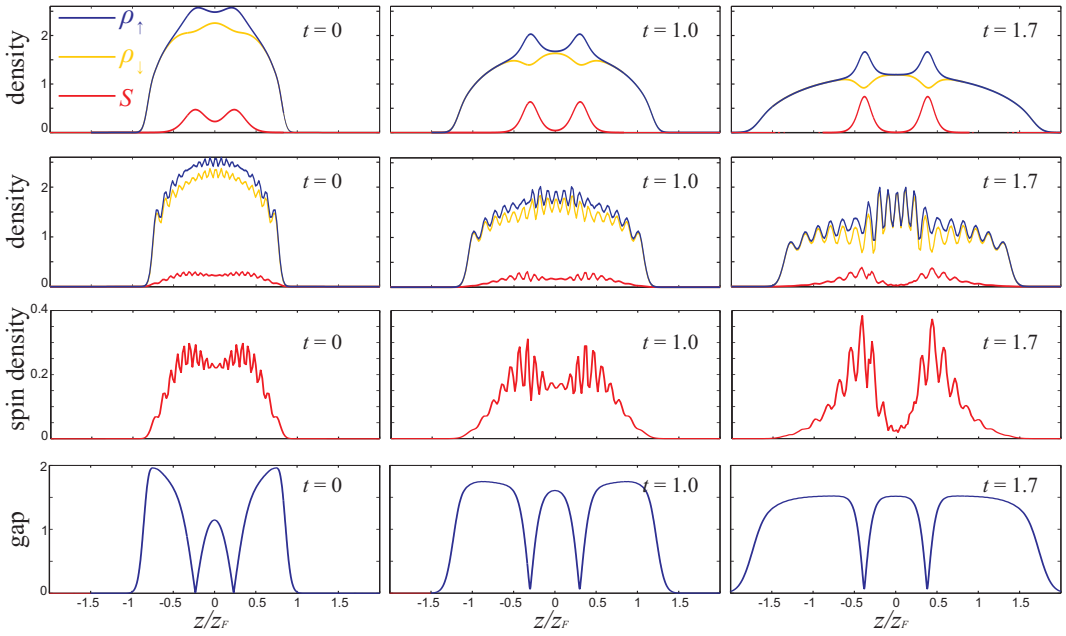

Figure 3.6: The expansion of sample with $N = 40$, $g_{1D} = -8.0$ and $P = 0.05$ which is below $P_c \approx 0.1$. Adopted from Ref. [29]. From left to right, each column represents snapshots of the expansion dynamics at t=0.0, 1.0, 1.7 ($1/\omega_z$). Row 1 displays the density profiles. In each plot, we show $\rho_\uparrow, \rho_\downarrow$ and $S = \rho_\uparrow - \rho_\downarrow$ obtained from BdG calculation. Row 2 is the same as Row 1 except that the results are obtained from TEBD calculation. Row 3 shows the spin densities $S(z)$ from the TEBD. Finally in Row 4 we plot the amplitude of the superfluid gap $|\Delta|$ from the BdG calculation.

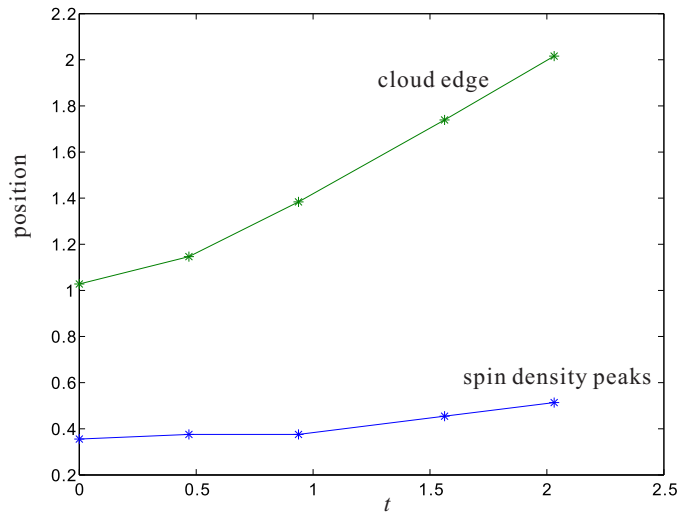

Figure 3.7: The positions of cloud edge and spin density peaks during expansion for $N = 40$, $P = 0.05$ and $g_{1D} = -8.0$.

edges. Here the BdG calculation tells us that there is exactly one excess spin bound to each of the nodes of the order parameter and the FFLO state is analogous to a band insulator of the *relative motion* between the unpaired and paired particles. The ground state represented in Fig. 3.6 is within this regime and spin density peaks represent the localization of unpaired spins at the nodes of Δ. During the time of flight, the excess spins are kept pinned to the nodes of the order parameter and become more tightly bound. The dramatic effects observed occur when this localization couples with the average enhancement of $|\Delta|$ implied by an increasing γ as the density drops during expansion [see Eq. (3.2)]; a uniquely 1D phenomenon. Henceforth we refer to these spin peaks as node signatures.

For $P > P_c$, the FFLO state still remains at the center in the ground state, but the wings exclusively contain the majority spin component. In this regime, there are more excess

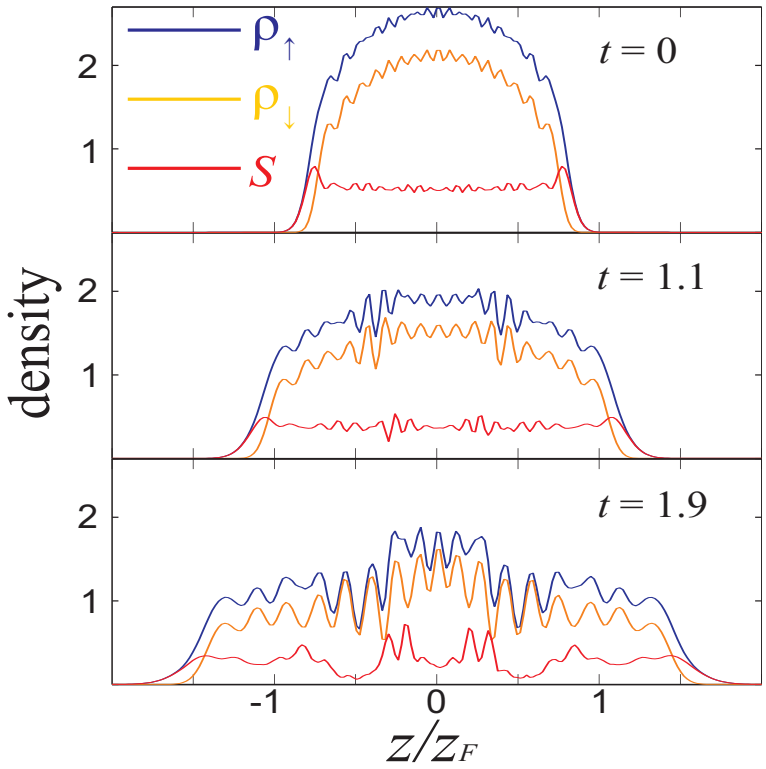

Figure 3.8: Density profiles, obtained from TEBD calculation, during the expansion of a sample with $N = 40$, $g_{1D} = -8.0$ and $P = 0.15$, which is above $P_c \approx 0.1$. Adopted from Ref. [29].

spins than nodes of Δ, and consequently they are less tightly bound. Here we expect the node signatures to be less dramatic which is confirmed in Fig. 3.8. In particular, the spin peaks near the edges are not well resolved. We can therefore conclude that the best place to observe the node signature is at $P < P_c$, where the signal is enhanced by both a large separation of the nodes and greater contrast with the background density. We note that, in weakly-interacting regime, the value of P_c increases with $|g_{1D}|$ up to a maximum $P_c = 0.2$ as shown in Ref. [62], implying a sizable observation window for the strong interactions

with which experiments are conducted.

At equilibrium, the FFLO correlation appears as peaks in the pair-momentum distribution n_k defined by:

$$n_k = \frac{1}{L} \int \int dz dz' \, e^{ik(z-z')} \, O(z, z') \,, \tag{3.39}$$

where $O(z, z') \equiv \langle \psi_\uparrow^\dagger(z) \psi_\downarrow^\dagger(z) \psi_\downarrow(z') \psi_\uparrow(z') \rangle$ is the two-point correlation function. In Fig. 3.9, we observe the effects of interaction on this signature during the expansion. The $t = 0$ curve represents n_k for the trapped ground state. One can clearly see that the n_k peaks at $q_0 = |k_\uparrow - k_\downarrow|$ as expected for an FFLO state. Furthermore we should expect $q_0 \approx \pi/d$, where d is the distance between two peaks in density profile, roughly corresponding to the half wavelength of the FFLO oscillation. For instance, for $N = 40$, g_{1D} and $P = 0.05$, we observe that $d \approx 0.6 Z_F$, and thus $\pi/d \approx 0.6$ in the trap units, which matches very well with the peak position $q_0 \approx 0.08 k_F$ as shown in the upper panel in Fig. 3.9. This reflects the fact that the extra spins tend to be localized at the nodes of the mean-field gap as shown in Fig. 3.6. However, after the expansion starts, the peaks diminish continuously as a result of interaction. After a sufficiently long time [90], n_k no longer possesses the observable peaks at finite momentum. In order to observe the peaks at finite momentum during expansion, one needs to shield the effect of the interaction between pairs. In principle, this can be achieved by suddenly increasing interaction strength g_{1D}, so the pairs are tightly bound and interaction between pairs becomes negliable. However, simulating such process within TEBD scheme requires keeping a significant number of states to ensure fidelity of the calculation. Therefore a simulation of such scenario for a sufficiently long time period is

beyond the capability of our current numerical implementation of the TEBD method.

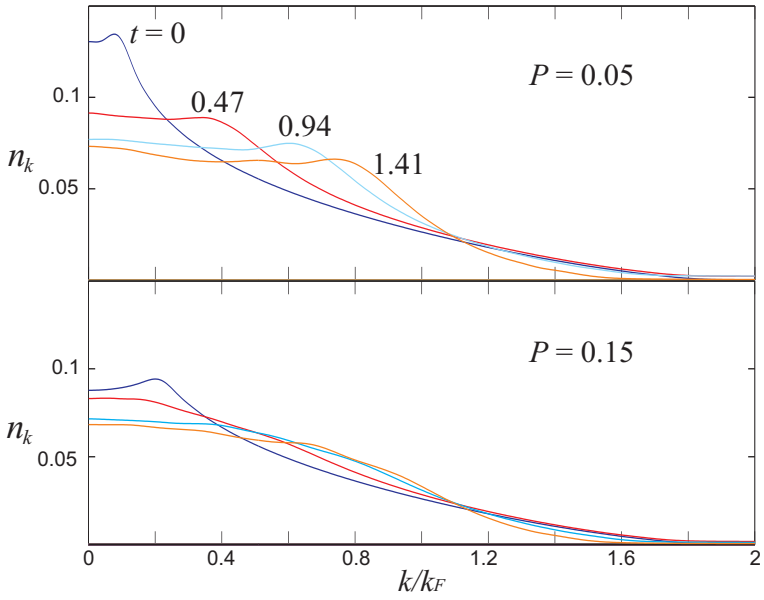

Figure 3.9: Pair momentum distribution at two different polarization for $g_{1D} = -8$ and $N = 40$. In each panel, we display n_k for different times. Counting from the left, the curves correspond to $t = 0$, 0.47, 0.94 and 1.41, from top to bottom. In both cases the momentum peaks representing the FFLO state disappear from the plot during the expansion. Adopted from Ref. [29].

One may wonder whether the node signatures can be observed in *in situ* density profiles of a trapped cloud with sufficiently large interaction strength. To answer this, we show in Fig. 3.11 the density profiles of a trapped system for $g_{1D} = -8$, -20 and -36. (Note that for the experiment reported in Ref. [26], $g_{1D} \sim -50$ for the central tube.) One can see that the modulation depth of the spin density of a trapped cloud is not very sensitive to g_{1D}. This is in sharp contrast to the BdG calculation where the spin density modulation is indeed enhanced as γ is increased as shown in Fig. 3.10 — an indication of the invalidity

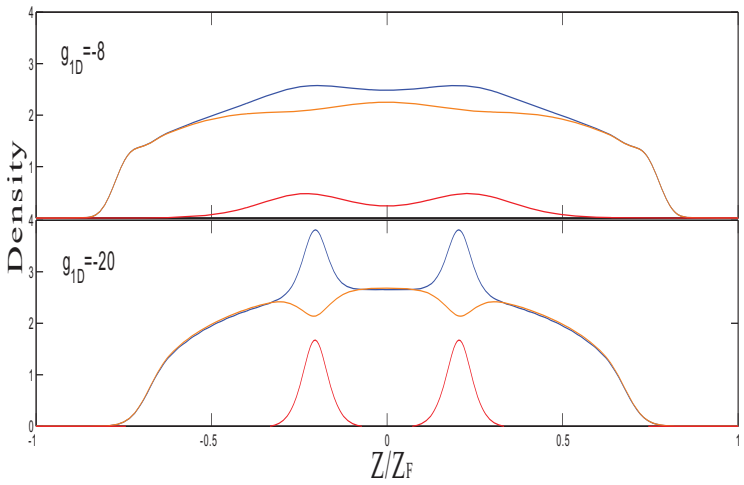

Figure 3.10: Ground state density profiles in trap, with $N = 40$, $P = 0.05$ and for different interaction strengths $g_{1D} = -8$ and -20 while the BdG calculation was not able to obtain faithful ground state for $g_{1D} = -36$. In each plot, we show $\rho_\uparrow, \rho_\downarrow$ and S obtained from mean-field BdG calculation.

of the mean-field theory for strong interaction. In the TEBD calculation, the localization of excess spin at large $|g_{1D}|$ is counter-balanced by increased quantum fluctuations neglected in the mean-field theory. Therefore, the dramatic emergence of node signatures is a unique feature of the expansion dynamics.

Finally, we address the question of the effect of the interaction strength in Fig. 3.12, where the spin densities in an expanding cloud are shown for two sets of interaction strength. Though the results for strong and weak interactions are qualitatively similar, the spin peaks start to develop earlier for the case of smaller g_{1D}. This could play an important role in practice when the finite lifetime of the system must be taken into account.

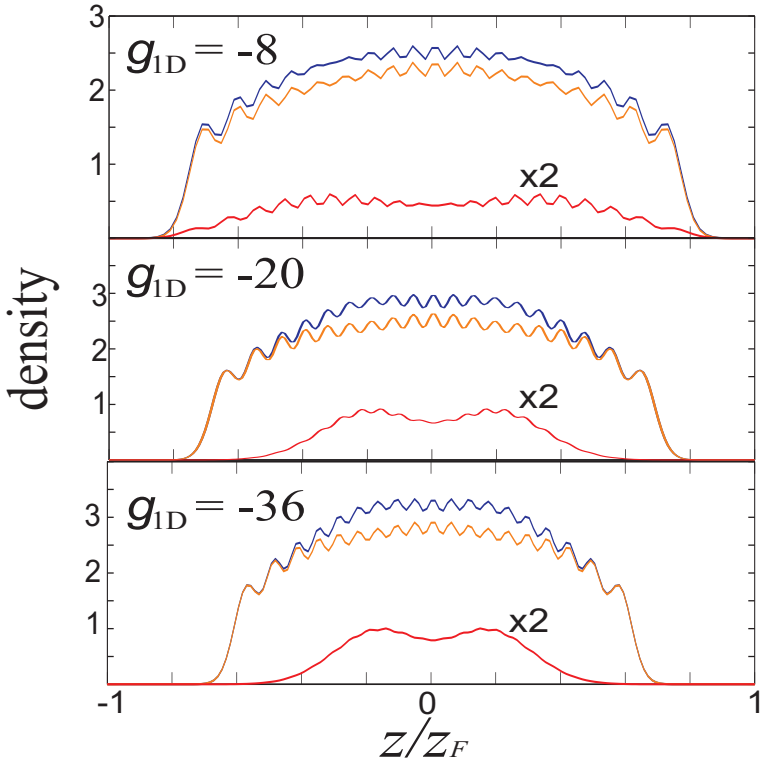

Figure 3.11: Ground state density profiles in trap, with $N = 40$, $P = 0.05$ and for different interaction strengths g_{1D}. In each plot, we show $\rho_\uparrow$, $\rho_\downarrow$ and S obtained from TEBD calculation. For clarity, the spin density S is magnified by a factor of 2. Adopted from Ref. [29].

3.5 Spin transport through ultracold Fermi gases in a harmonic trap

The TEBD scheme we discussed above provides us with a powerful and numerically accurate tool to investigate the dynamics of 1D strongly interacting systems. Using the TEBD method, we are able to characterize the states of matter by studying important dynamical properties such as spin transport. This section is devoted to a study aiming at gaining a

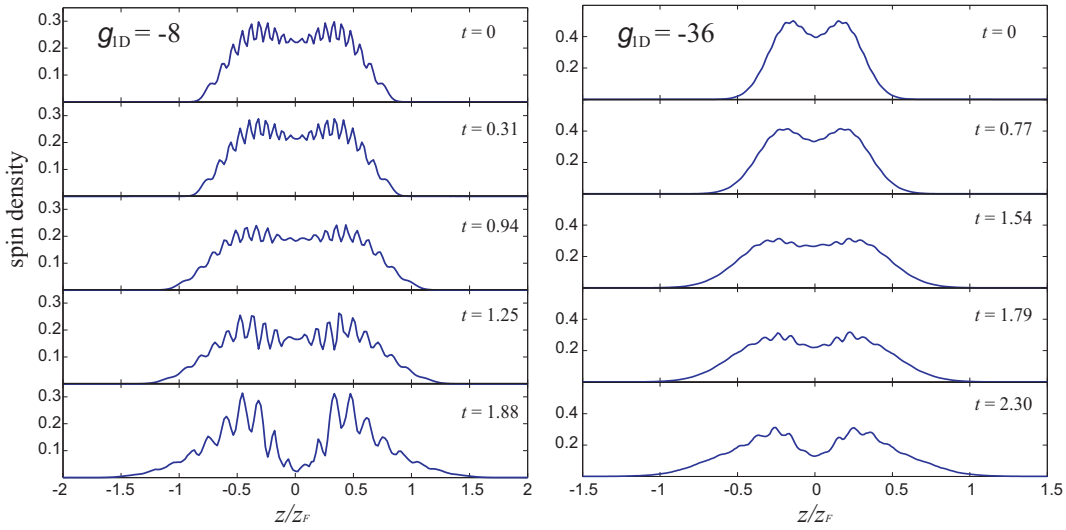

Figure 3.12: Expansion profiles for two different samples with $N = 40$, $P = 0.05$ but at different interaction strengths g_{1D}. In each plot, we plot the TEBD result for S. In both cases, the modulation depth of the spin density first reduces and then strengthens during expansion. Adopted from Ref. [29].

deeper understanding of the pairing mechanism. We achieve this with a numerical study of spin transport in 1D trapped cold atoms using the TEBD method. With a series of simulation of transporting a single spin through different stationary states at the center of the harmonic trap, we study how the pairing between the two spin components is affected by the population imbalance and interaction strength in the two-component fermionic systems. Still we consider that these two fermionic component interacts only via inter-species contact interaction, therefore the system can be fully characterized by the 1D coupling parameter g_{1D} as before. The initial states in our experiment is built in the following way: a ground state of interest at the center of the harmonic trap is obtained by imaginary time evolution using TEBD method. Then at t=0 we let a spin-↑ particle , which is used as a probe and originally located at the edge of the trap, start to move freely towards the central state under the influence of harmonic trapping potential and this probe spin will interact with the central stationary state after reaching the trap center. The real-time evolution of the whole sytem can be reliably emulated by using TEBD simulation. We perform a systematic and comparative simulation by initially placing different trapped ground state at the trap center. The four representative stationary state we choose are following: a trapped ground state of (I) a single spin-↓ particle, (II) a single pair of particles (↑↓), (III) two spin-↓ particle (↓↓) and (IV) three particles with a configuration (↓↑↓). Also we will present an on-going study of transporting the probe spin through the population imbalanced ground state that we discussed in the previous section of this chapter.

3.5.1 Case I:

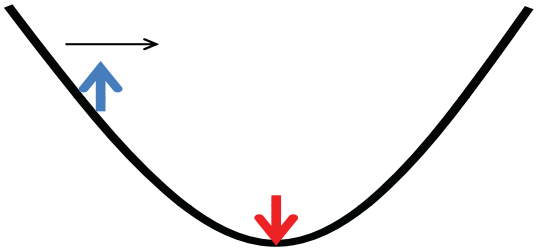

Figure 3.13: Schematic diagram of the experimental setup of case (I)

We start with a benchmark study of case (I), where a spin-↑ probe particle collides with a spin-↓ particle initially at rest at the trap center. This problem can be effectively treated as a single-particle problem as the center-of-mass motion and the relative motion can be decoupled [97, 98, 99]. Starting from the Hamiltonian for two distinguishable fermions denoted as spin-↑ particle and spin-↓ particle as follows.

$$H = -\frac{\hbar^2}{2m}\sum_{\sigma=\uparrow,\downarrow}(\frac{d^2}{dz_\sigma^2} + \frac{1}{2}m\omega_z^2 z_\sigma^2) + g_{1D}\delta(z_\uparrow - z_\downarrow) \tag{3.40}$$

which can be separated into the center-of-mass part H_c and relative motion part H_r:

$$\begin{aligned} H_c &= -\frac{\hbar^2}{2M}\frac{d^2}{dR^2} + \frac{1}{2}M\omega_z^2 R^2 \\ H_r &= -\frac{\hbar^2}{2\mu}\frac{d^2}{dr^2} + \frac{1}{2}\mu\omega_z^2 r^2 + g_{1D}(r)\delta(r) \end{aligned} \tag{3.41}$$

where the new coordinates $R = (z_\uparrow + z_\downarrow)/2$ and $r = z_\uparrow - z_\downarrow$ and the reduced mass $\mu = m/2$ while $M = 2m$ is the total mass. Correspondingly the wavefunction of the system can be

decomposed into the form as follows:

$$\Psi_{\uparrow\downarrow}(z_\uparrow, z_\downarrow) = \Psi_c([z_\uparrow + z_\downarrow]/2)\Psi_r(z_\uparrow - z_\downarrow) = \Psi_c(R)\Psi_r(r) \tag{3.42}$$

where Ψ_c and Ψ_r are the wavefunctions in center-of-mass and relative motion coordinates respectively. Since it is easy to see that Ψ_c will be under simple harmonic oscillation in the center-of-mass frame, we just need to focus on the part Ψ_r, whose effective potential can be reduced to be a 1D harmonic oscillator in addition to a delta potential $g_{1D}\delta(r)$ as shown in Eq. (3.41).

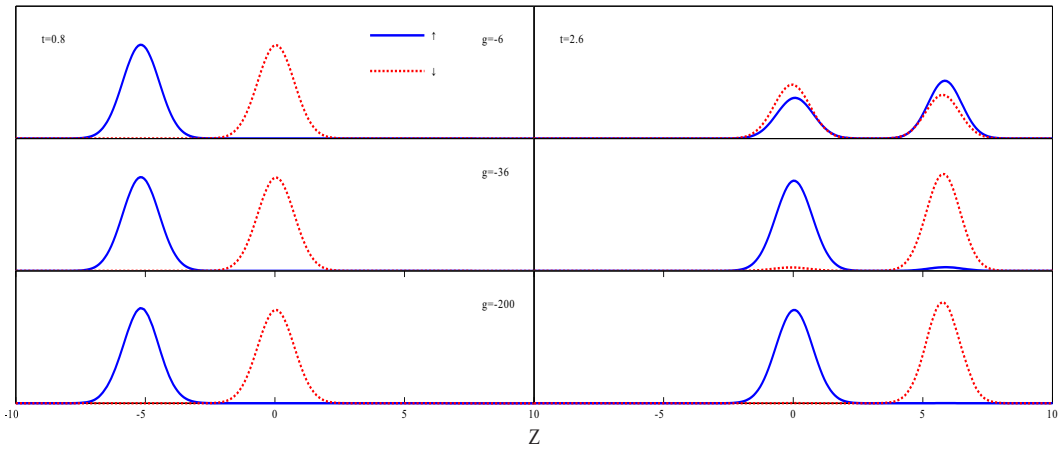

Figure 3.14: From top to bottom: time evolution of the density profile for $g_{1D} = -6, -36$ and -200 for case I. The trap is centered at $z = 0$. Representive snapshots are taken at $t = 0.8$ (left column) and 2.6 (right column) respectively.

The evolution of the system can be obtained by solving the 1D time-dependent Schrödinger equation (TDSE) numerically with the delta potential modeled by a narrow Gaussian, which provides us with a good basis for benchmarking the TEBD results based on the full two-body Hamiltonian. In Fig 3.14, we show the evolution of the system calculated by

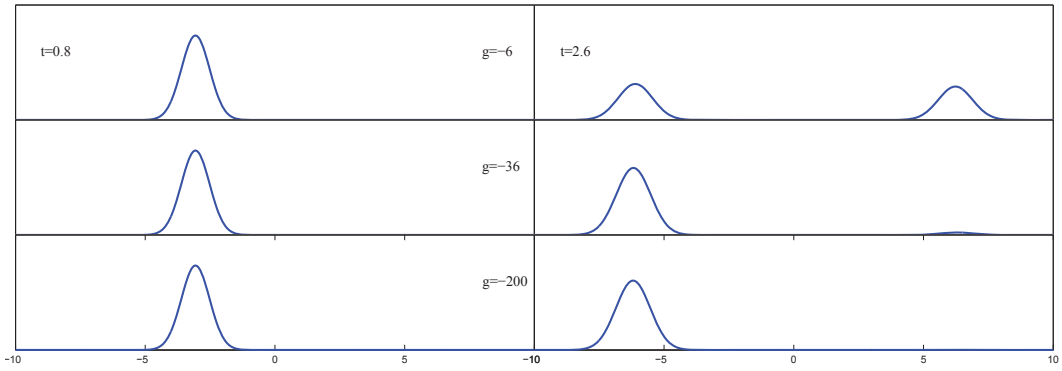

Figure 3.15: Solution of single-particle TDSE in the relative motion coordinate, from top to bottom, snapshots showing the transmission/reflection when $g_{1D} = -6, -36, -200$.

the TEBD method for various attractive interaction strengths $g_{1D} = -6, -36$ and -200. A strikingly interesting phenomenon found here is that at strong attractive interacting strength $g_{1D} = -200$, the collision between the two particles behave like that between two classical billiard balls. The incoming spin-↑ particle reaches the bottom of the trap, collides with and transfers all its momentum to the initially stationary spin-↓ particle. And the incoming spin-↑ particle will remain at bottom trap center after the collision. This complete elastic collision would correspond to a total reflection of the wave packet Ψ_r by the delta potential in the relative motion frame, which has been confirmed with the solution of TDSE as shown in the Fig. 3.15. Furthermore, the TDSE solution confirms that the total reflection happens for $|g_{1D}| = 200$ no matter whether the interaction is attractive or repulsive. It is well known that when plane waves are scattered by a delta potential in 1D, the reflection/transmission coefficients are independent of the sign of the delta potential. However, it is not obvious that the same relation can be extended to our case if we consider a Gaussian wavepacket

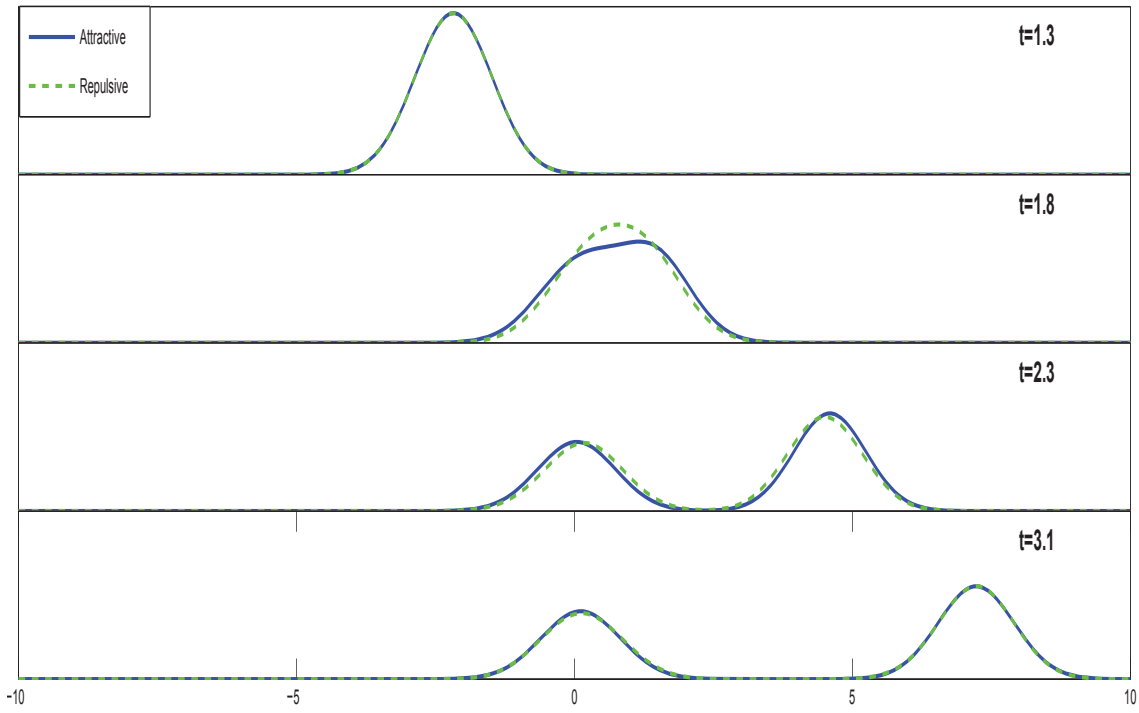

Figure 3.16: Time evolution of spin-↑ particle in the repulsively and attractively interatintg case for $|g_{1D}| = 6$ calculated by TEBD method. The trap is centered at $z = 0$. From top to bottom, representive snapshots taken at $t = 1.3, 1.8, 2.3$ and 3.1.

scattered by a delta potential with the presence of a harmonic trap. By using the propagator for Gaussian wavepacket, it can be shown in a homogeneous system [102] that the wave packet reflection/transmission coefficients are the same as that of plane wave after a long time, and hence is independent of the sign of the delta potential. Although this fact is difficult to be confirmed with the TDSE calculation due to the numerical errors caused by the finite width of the narrow Gaussian potential we used to emulate the delta potential, our TEBD calculation has verified this as shown in Fig. 3.16. When the interaction

strength is reduced, Ψ_r will experience partial reflection as shown in Fig. 3.14. Again it is in full agreement with the TDSE results. Overall in this benchmarking case we show that TEBD results have a good agreement with the single-body TDSE solution on how the two distinguishable fermions will interact with each other under harmonic trapping.

3.5.2 Case II:

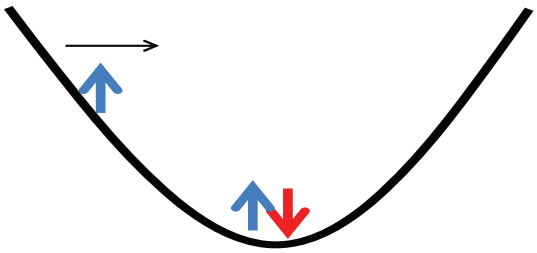

Figure 3.17: Schematic diagram of the experimental setup of case (II)

We now move on to case (II), to find out how a pair of spin-↑ and spin-↓ particles that originally stays in its ground state at the center of the harmonic trap will be affected when the incoming spin-↑ particle collides with it. To characterize the effect of the interaction strength, we keep track of the density variation of the spin-↓ particle by recording its peak value as a function of time. As shown in the Fig. 3.18, the density maximum of the spin-↓ particle for $g_{1D} = -6$, a weak interaction strength, experiences much stronger variation during the whole process comparing with the intermediately interacting case at $g_{1D} = -36$ and the strongly interacting case at $g_{1D} = -200$. Furthermore, we observe that the pattern of the time-varying density maximum of spin-↓ is very similar for intermediately and

strongly interacting cases, in which a dip shows up when collision happens between the pair and incoming spin-↑ particle. This is strikingly different for the weakly interacting case, in which a peak appears instead. The behavior at weak interaction strength can be intuitively understood: due to the attractive interaction between spin-↑ and spin-↓ particles, when the incoming spin-↑ reaches the bottom of the trap, the spin-↓ particle experiences an enhanced attractive interaction. Hence its peak density increases. The counter-intuitive behavior at stronger interaction strength can be understood as follows: when the interaction strength increases, the pair originally staying at the center of the trap is tightly bounded as a bosonic molecule. The collision process should really be understood as a collision between the incoming spin-↑ particle with the bosonic molecule. That a small dip appeared in the peak density of spin-↓ particle at $g_{1D} = -36$ and -200 indicates that the interaction between the spin-↑ particle and the bosonic melecule is weakly repulsive. It might be reasonable to speculate that there exists a critical interaction strength above which the system becomes 'repulsive' and the pair is less affected during the passing through than in the weakly interacting case. The representative snapshots at $t = 1.3, 1.5, 1.8$ and 2.0 for three interaction strengths are shown in the Fig. 3.19.

3.5.3 Case III:

We move our exploration forward to case (III) with two originally stationary spin-↓ particles at the center of the trap. We first look at the strongly interacting system, $g_{1D} = -200$. As shown in the Fig 3.21, we find that after the collision, the momentum of the incoming

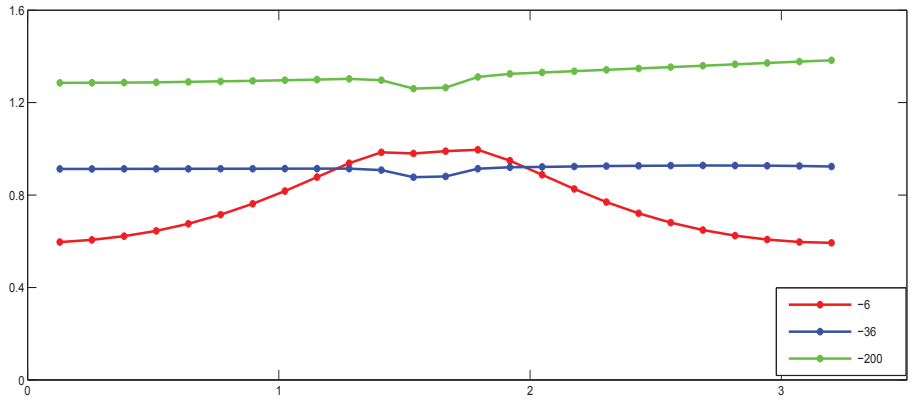

Figure 3.18: Evolution of the density maximum for the spin-↓ particle for $g_{1D} = -6, -36, -200$.

spin-↑ particle is entirely transferred to one of the spin-↓ particles, which will be knocked out and move towards the edge of the trap, while the incoming spin-↑ will be stopped at the center of the trap. This process is similar to an elastic collision seen in classical system. Again the system appears to be repulsive with the strong interaction strength. The two particles (one spin-↑ and one spin-↓) remaining at the center of the trap are separated from each other, indicating that they are not paired as usually expected from a strongly attracted pair. The two particles staying at the center of the trap are therefore in a highly excited state. This is because that the full pairing between spin-↑ particle and spin-↓ particle with strongly attractive interaction, $g_{1D} = -200$ leads to significant lowering in the energy and thus the extra energy needs to be expelled from system due to requirement of energy conservation. Since such energy dissipation mechanism is absent, the full pairing cannot happen between the ↑ and ↓ spin. As a consequence, this procedure allows us to create excited states in a controlled way.

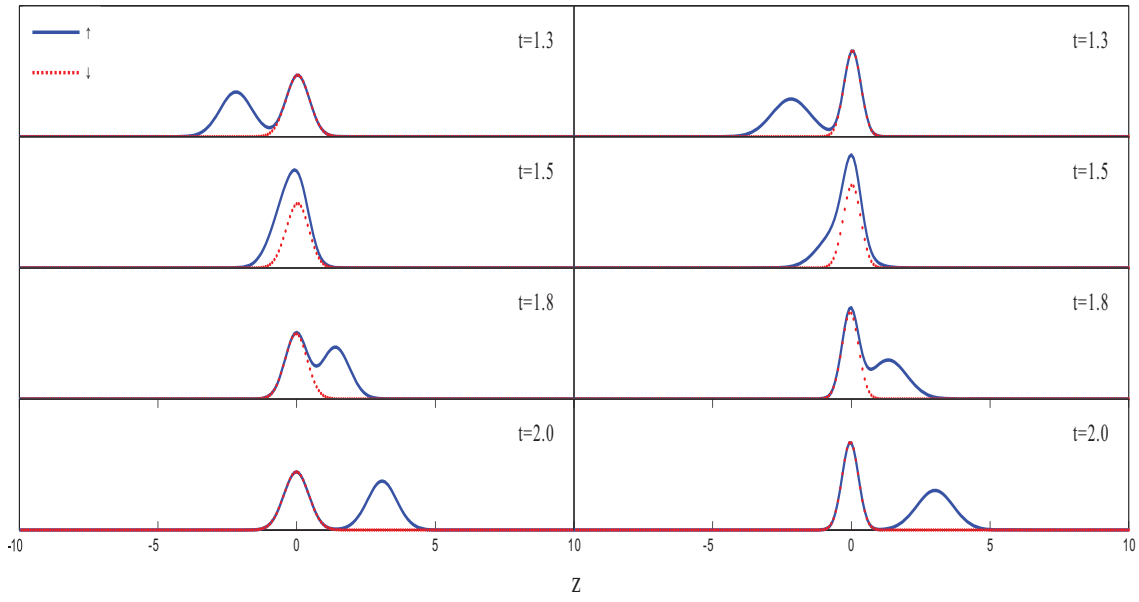

Figure 3.19: Time evolution of the density profiles for case II. The trap is centered at $z = 0$. Left column: $g_{1D} = -6$, right column:$g_{1D} = -200$. Representive snapshots are taken at $t = 1.3, 1.5, 1.8$,and2.0 respectively.

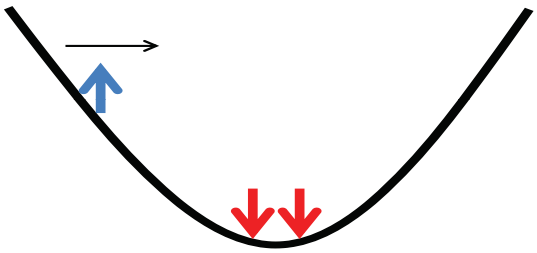

Figure 3.20: Schematic diagram of the experimental setup of case (III)

Now let us describe the situations with lower interaction strengths. As shown in the Fig. 3.21, significant difference shows up when the interaction strength is lower to $g_{1D} = -6$. We can find that the wavepacket of the spin-↑ particle partially transmits through and mixes with wavepacket of the spin-↓ particles. The partial wave packets of both spin components travel forward together while the remaining wave packets at the center of the trap keep changing with time indicating that it is left in a non-stationary state, which is dramatically different from the observation in the cases with stronger interaction strengths.

3.5.4 Case IV:

In this case, an imbalanced configuration ↓↑↓ is initially prepared at the center of the trap. In the strongly interacting case, $g_{1D} = -200$, the incoming spin-↑ knocks out one spin-↓ particle entirely (shown in the right column in Fig. 3.23) and a new configuration ↑↓↑ forms and remains at the center. This is very similar to what we have seen in case III and the underlying physics in both cases is different from that in case II. The kinetic energy carried by the incoming spin-↑ particle is transferred to the knocked out spin-↓ particle.

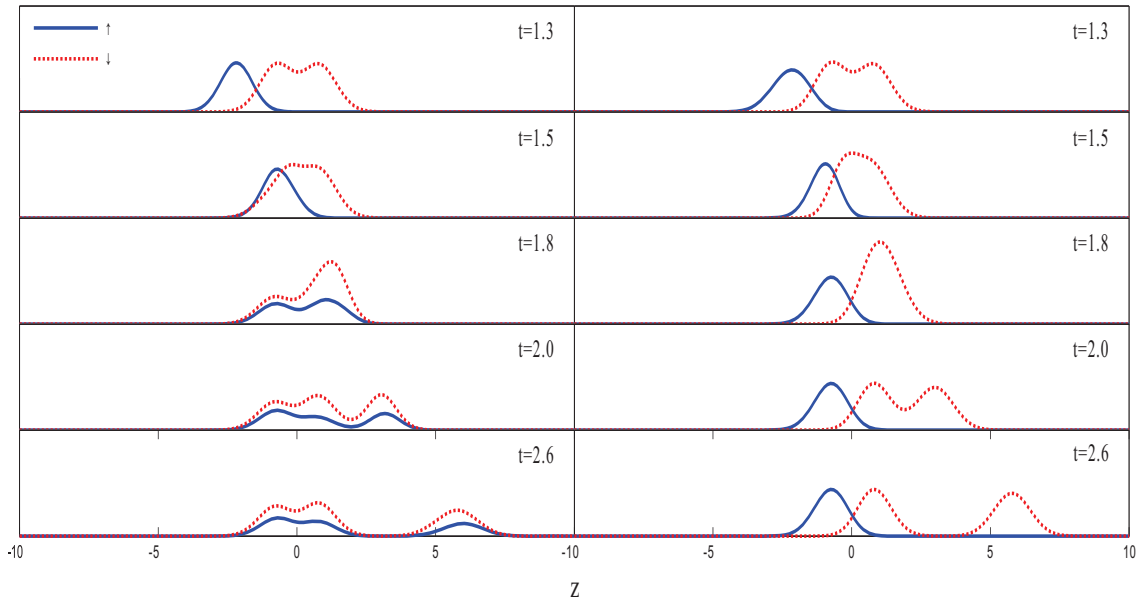

Figure 3.21: Time evolution of the density profiles for case III. The trap is centered at $z = 0$. Left column: $g_{1D} = -6$, right column:$g_{1D} = -200$. Representive snapshots are taken at $t = 1.3, 1.5, 1.8, 2.0, 2.6$ respectively.

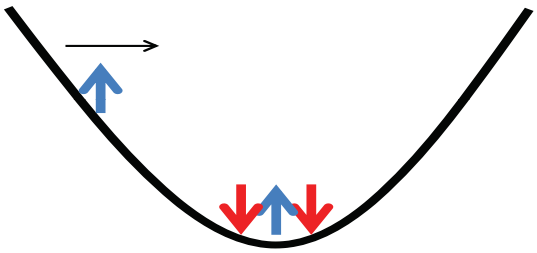

Figure 3.22: Schematic diagram of the experimental setup of case (IV)

From the symmetry between the spin-↑ particle and spin-↓ particle, it is easy to see that the system conserves the energy. In the weakly interacting limit, $g_{1D} = -6$, similarly the incoming spin-↑ wave packet partially transmits (as shown in the left column in Fig. 3.23). And a part of the wave packets of both the spin-↑ particles and spin-↓ particles continue to move towards the edge of the trap. The fully pairing between the two spin-↑ particles and the two spin-↓ particles is again prohibited by the requirement of the energy conservation.

3.5.5 Case V

At last, we show the preliminary result of the transport of a single spin-↓ particle through a population imbalanced state we discussed in the previous part of this chapter. Here we consider a partially polarized ground state of 40 particles sitting at the center of the trap. The polarization of the system is $P = 0.05$, consisting of 21 spin-↑ particles and 19 spin-↓ particles, and here the coupling parameter is $g_{1D} = -36$. Again we observe similar dynamics as shown in case IV, that is, the incoming minority spin-↓ particle knocks out a

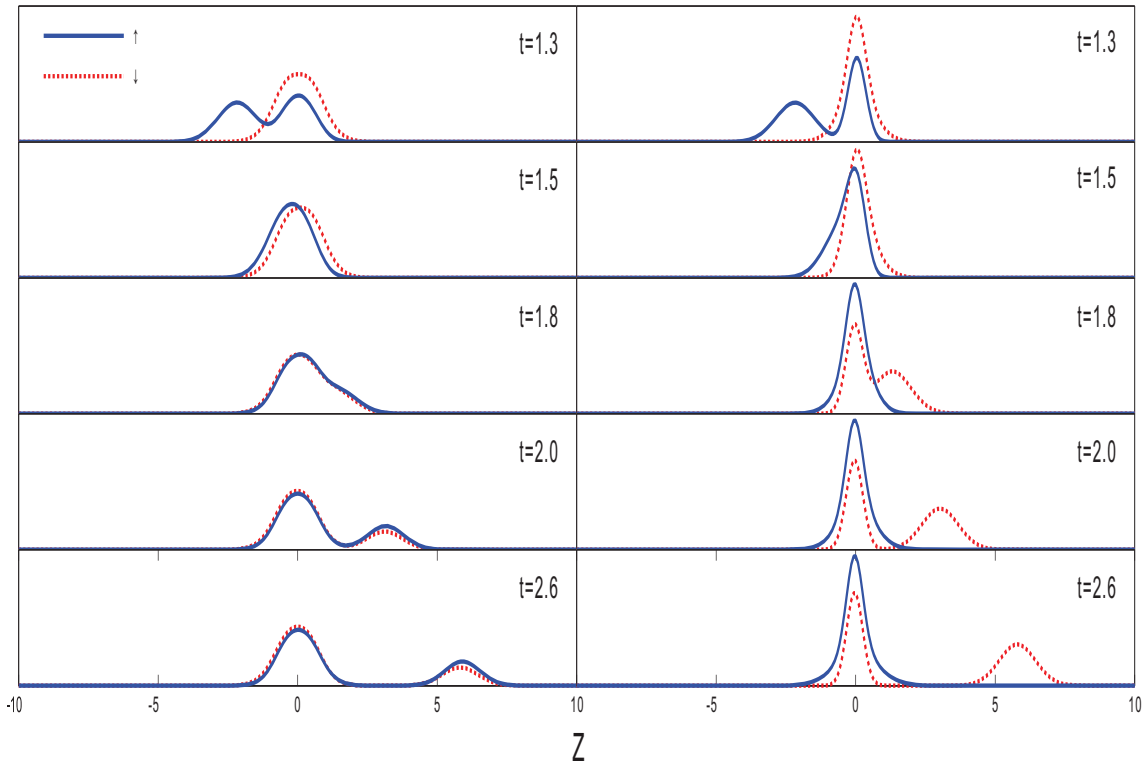

Figure 3.23: Time evolution of the density profiles for case IV. The trap is centered at $z = 0$. Left column: $g_{1D} = -6$, right column:$g_{1D} = -200$. Representive snapshots are taken at $t = 1.3, 1.5, 1.8, 2.0$ respectively.

majority spin-↑ particle entirely. As a result, after the collision, the central state becomes population balanced with 20 particles in both spin-↑ and ↓ component. It is easy to see that such state is still not in its ground state due to energy conservation constraint. This observation is consistent with the results we presented above. However, by using this trapped partially polarized ground state as the central stationary state, we may consider some more intersting scenarios, such as using the majority spin-↑ particle as the probe spin. We can also initially place a ground state with a polarization above P_c at the trap center. Results of these on-going investigations will be reported in other places.

In summary, we carried out systematic numerical experiments studying the transport dynamics of a single spin in trapped two-component systems with only a few particles, which deepens our understanding of the pairing mechanism. Recent advancements in experiment techniques have made ultracold Fermi gas an ideal laboratory to investigate interesting physics in few-particle system[100]. Experimentalists have been able to prepare the ultracold few-particle samples in traps with high fidelity [100, 101]. Therefore our proposed scheme is feasible to be implemented with currently available experimental technology. The major observation from our simulation shows that the spin transport dynamics is very sensitive to the interaction strength as well as population difference. Therefore it can serve as a powerful tool to investigate the novel properties of quantum gases.

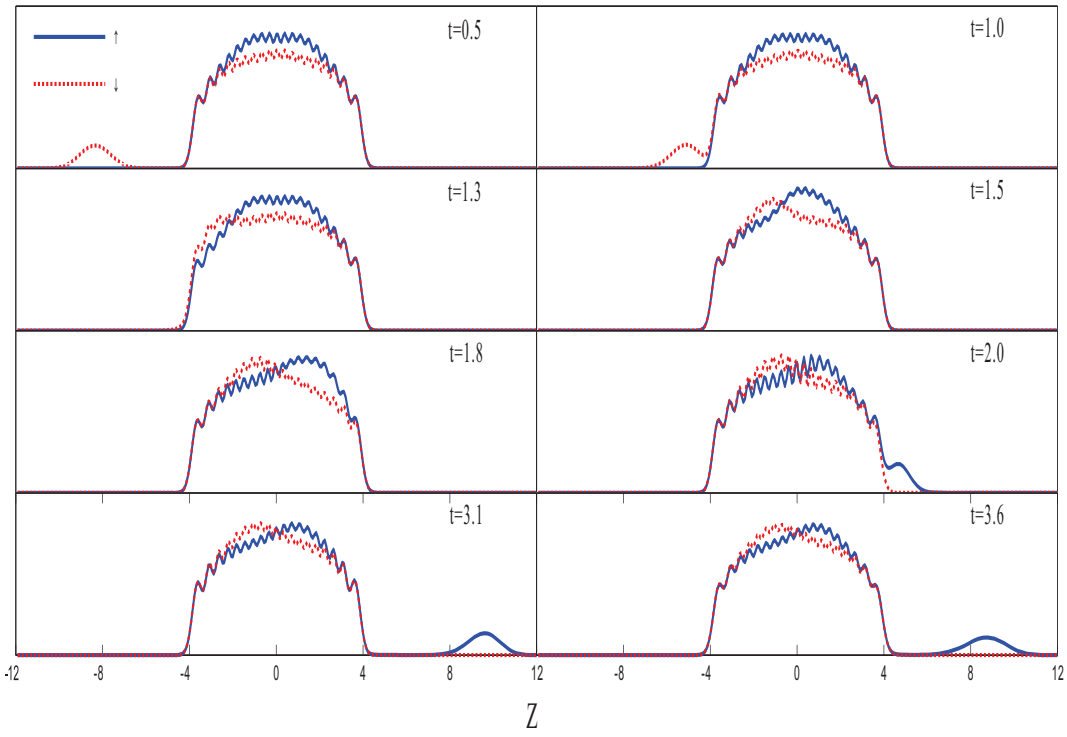

Figure 3.24: Time evolution of the density profiles for case V. The trap is centered at $z = 0$. The trapped ground state intially staying at the center of the trap consists of 21 spin-$\uparrow$ and 19 spin-$\downarrow$ particles and $g_{1D} = -36$. Representive snapshots are taken at $t = 0.5, 1.0, 1.3, 1.5, 1.8, 2.0, 3.1$, and 3.6 respectively.

Chapter 4

Conclusions

The evidence of the FFLO phase, a novel type of superfluid, which has been intensively searched for in various condensed matter systems, still remains elusive. The utilization of cold atom system provides us with a unique opportunity for the experimental verification of such exotic phase. In this thesis, we have pesented a numerical study focused on the search of FFLO states in ultracold polarized Fermi gases. We have employed several numerical techniques, which range from mean-field level to quasi-exact calculation of many-body states. The results we have obtained not only can help the understanding of the underlying physics of diversified experimental observations, but also can help guide future experiments for the direct evidence of the FFLO phases.

The trapping geometries may create theoretical difficulities in clearly understanding the results of cold atom experiment. The effective chemical potential μ varies in space, and several phases may co-exist within a trapped sample. In order to explore the phase diagram

of trapped cold atom samples and motivated by the Rice experimental results, we carried out a systematic study of trapped 3D Fermi gases in the unitary limit which is presented in Chapter 2. By starting from different initial ansatz, we are able to arrive and identify three categories of solutions through a self-consistently solution of the BdG equations using state-of-the-art numerical techniques. For large particle numbers, the class of LDA-like solution always has the lowest energy in our calculations. However, the validity of the LDA is also sensitive to the trap geometry: Traps with small anisotropy favor the LDA. Our calculations show that for a relatively small number of atoms in a very elongated trapping potential, the system contains three phases: an unpolarized BCS phase, a partially polarized FFLO-like phase and a normal phase. That the FFLO region exists may be understood from the view point of reduced effective spatial dimension. As N is increased while all other parameters remain fixed, the FFLO-like region eventually disappears. Starting from engineered gap ansatz with spatial modulations, the iterative solution chooses between two stationary points, which are not necessarily the global free energy minimum, but each of which features density profiles strikingly similar to experimental observations at Rice. The most likely solution which is consistent with the Rice experiment is a metastable state that supports a partially polarized superfluid phase strikingly similar to the FFLO phase. This state becomes increasingly robust as trapping geometry becomes more elongated. Even within a trapped environment, the nodes of the order parameter in the FFLO-like phase are radially aligned which, with low enough noise, leave an accessible signal in axial spin density $\delta\rho_{1d}$.

As predicted in theory, polarized Fermi gases in lower dimensions are much more promising for observing the FFLO state directly. Although the Rice's experimental realization of 1D polarized Fermi gases has shown exciting agreement with the theoretical forecasting, further verification of the existense of the FFLO states is still needed. It has been proposed that such confirmation might come from the time-of-flight experiment, which is a powerful and straightfoward tool to study cold atom systems. Different from many other proposals relying on inference effect, our results predict that strong spin density modulations, which can be readily observed in experiment, emerge during the expansion and provide direct evidence of the FFLO state. Experimentally, an array of 1D tubes are created [26] and the measurement averages over different tubes. One obvious concern is that such an average may smear out the spin modulation. Although a full investigation of the dynamics of coupled tubes lies outside of the scope of the current work, we comment that this problem can be mitigated by allowing small inter-tube tunneling such that a quasi-1D situation results. The BdG studies in both a 3D cigar-shaped trap as discussed in chapter 2 and coupled 1D tubes [103] have shown that the nodes of the order parameter (and hence the spin peaks) tend to align along the radial direction. Thus the node signature would not be smeared out by averaging. Apart from the pair-momentum distribution function described in Chapter 3, other methods [91] have been proposed in the literature to detect FFLO. However, they all rely on interferometric techniques requiring two fermionic superfluids, one of them being the FFLO state. Our proposal, in contrast, only requires the FFLO cloud itself and hence is significantly simpler.

On the other side, the numerical schemes we have built and implemented in this thesis can be readily extended to the studies of many scenarios for exploring the interesting physics in ultracold quantum gases. The BdG equation has been employed as a powerful tool to investigate imhomogenous superconducting states in condensed matter physics for a long time and proved as a sophisticated method which has generated many signicant results, and its extension to cold atom systems is seamless. The parallel solver we developed for BdG equations enable us to expand our research scope in a ready manner. For instance, given a particle number N, we can study the 3D-1D dimensional crossover by increasing trap aspect ratio α continuously until the system reaches the 1D regime eventually. A 3D time-dependent BdG code can be used to study the expansion dynamics of coupled tubes simulating the realistic experimental configuration. The TEBD method, as demonstrated in Chapter 3, is a 'quasi-exact' numerical algorithm for strongly interacting many-body system in 1D especially suitable for simulating the dynamics. As we know, a lot of interesting physics in ultracold quantum gases can be explored through the time-of-flight, transport and quench processes, and the TEBD method thus is one of the most powerful numerical tools for our future investigation of such 1D systems. Furthermore, we should continue to utilize strategy combining the mean-field BdG studies with the TEBD scheme for 1D systems. Although BdG approach, generally speaking, cannot deliver quantitatively accurate results, as a mean-field method, it is computationally much more efficient than the TEBD method and can provide additional insights. Within the BdG scheme, it is feasible to construct a phase diagram by scanning the whole parameter space. Then we can employ

the TEBD scheme to obtain the quantitatively reliable results under the guidance of such phase diagram.

Appendix A

Due to the assumption of contact interaction, the gap Δ is a function of the center-of-mass coordinate of the pair, $\vec{R}$. To discuss the regularization, it is more convenient to re-introduce back the relative coordinate $\vec{r}$, with which the gap is defined as

$$\Delta(\vec{R},\vec{r}) = \langle\psi_{\uparrow}(\vec{R}+\vec{r}/2)\psi_{\downarrow}(\vec{R}-\vec{r}/2)\rangle$$

which diverges as $\frac{\Delta(\vec{R})}{2\pi r}$ when $r \to 0$ [96]. To regularize Eq. (2.16), one simply subtracts off the $1/r$ divergence to obtain the regularized equation [96]:

$$\frac{\Delta(\vec{R})}{g} = \sum_{j} u_j(\vec{R})v_j^*(\vec{R})\, f(E_j) - \frac{\Delta}{2\pi r} \tag{4.1}$$

In practice, the convergene of the sum above is quite slow and we discuss here a numerically efficient way of evaluating $\Delta(\vec{R})$ to sufficient accuracy without undue effort. First an energy cutoff E_c is used to break the sum of Eq. (2.16) into two pieces as ff.

$$\frac{\Delta(\vec{R})}{g} = \sum_{E_j<E_c} u_j(\vec{R})v_j^*(\vec{R}) f\,(E_j) + \frac{\Delta_c(\vec{R})}{g} - \frac{\Delta(\vec{R})}{2\pi r} \tag{4.2}$$

The second term $\Delta_c(\vec{R})$ is an approximation to the sum above the cutoff using the LDA result for the pairing field [60] which can also be written as :

$$\frac{\Delta_c(\vec{R})}{g} = \frac{\Delta(\vec{R})}{(2\pi)^3}\int_{k_c}^{\infty}\frac{d^3k}{\sqrt{(\frac{k^2}{2}-\mu(\vec{R}))^2+\Delta^2}} \tag{4.3}$$

where k_c is the momentum cutoff related to E_c. This leads to a computationaly efficient form of the gap equation:

$$\frac{\Delta(\vec{R})}{U_{\text{eff}}(\vec{R})} = \sum_{E_j<E_c} u_j(\vec{R})v_j^*(\vec{R})\,f(E_j). \tag{4.4}$$

Here we have employed the identity:

$$\int_0^{\infty}\frac{d\vec{k}}{(2\pi)^3}\frac{e^{ikr}}{\frac{k^2}{2}} = \frac{1}{2\pi r} \tag{4.5}$$

to subsume the LDA approximation of the gap (Δ_c) into an effective interaction defined by:

$$\frac{1}{U_{\text{eff}}(\vec{R})} = \left[\frac{1}{g} - \int_{k_c}^{\infty} d^3k\left(\frac{1}{\sqrt{(\frac{k^2}{2}-\mu(\vec{R}))^2+\Delta^2}} - \frac{1}{\frac{k^2}{2}}\right)\right] \tag{4.6}$$

Bibliography

[1] Anderson, M. H., J. R. Ensher, M. R. Matthews, C. E. Wieman, and E. A. Cornell, Science **269**, 198 (1995).

[2] Davis, K. B., M.-O. Mewes, M. R. Andrews, N. J. van Druten, D. S. Durfee, D. M. Kurn, and W. Ketterle, Phys. Rev. Lett. **75**, 3969 (1995).

[3] Bradley, C. C., C. A. Sackett, J. J. Tollett, and R. G. Hulet, Phys. Rev. Lett. **75**, 1687 (1995).

[4] C.C. Bradley, C.A. Sackett, and R.G. Hulet, Phys. Rev. Lett. **78**, 985 (1997).

[5] DeMarco, B., and D. D. Jin, Science **285**, 1703 (1999).

[6] Truscott, A., K. Strecker, W. McAlexander, G. Partridge, and R. G. Hulet, Science **291**, 2570 (2001).

[7] F. Dalfovo, S. Giorgini, L. P. Pitaevskii, and S. Stringari, Rev. Mod. Phys. **71**, 463 (1999) and references therein.

[8] S. Giorgini, L. P. Pitaevskii, and S. Stringari, Rev. Mod. Phys. **80**, 1215 (2008) and references therein.

[9] L.N. Cooper, Phys. Rev. **104,** 1189 (1956)

[10] J. Bardeen, L. N. Cooper, and J.R. Schrieffer, Phys. Rev. **108,** 1175 (1957)

[11] A.J. Leggett. J. Phys. C. **41,** 7 (1980)

[12] P.Nozieres and S. Schmitt-Rink, J. Low Temp. Phys. **59,** 195 (1985)

[13] H. Feshbach, Ann. Phys. (N.Y.) **5**, 357 (1958)

[14] H. Feshbach, Ann. Phys. (N.Y.) **19**, 287 (1962)

[15] C. Chin, R. Grimm, P. Julienne and E. Tiesinga, Rev. Mod. Phys. **82,** 1225 (2010)

[16] Figure downloaded from http://atomcool.rice.edu/

[17] A.M. Clogston, Phys. Rev. Lett. **9,** 266 (1962)

[18] B.S. Chandrasekhar, App. Phys. Lett. **1,** 7 (1962)

[19] A.I. Larkin and Y. N. Ovchinnikov, Sov. Phys. JETP. **20,** 762 (1965)

[20] P. Fulde and R.A. Ferrel, Phys. Rev. **135**, A550 (1964)

[21] Y. Matsuda, H. Shimahara, J. Phys. Soc. Jpn. **76**, 051005 (2007) and references therein

[22] S. Uji et al. Nature **410**, 908 (2001)

[23] K. Izawa et al., Phys. Rev. Lett. **88**, 027002 (2002)

[24] D.E. Sheehy, and L. Radzihovsky, ANNALS OF PHYSICS **322.** 1790 (2007) and references therein

[25] H. Shimahara, THE PHYSICS OF ORGANIC SUPERCONDUCTORS AND CONDUCTORS, Springer Series in Materials Science **110,** 687 (2008)

[26] Y.-A. Liao, A. S. Rittner, T.Paprotta, W. Li, G. B. Partridge, R. G. Hulet, S. K. Baur, and E. J. Mueller. Nature (London) **467,** 567 (2010).

[27] L. O. Baksmaty, H. Lu, C.J. Bolech, and H. Pu, New J. Phys. **13,** 055014 (2011).

[28] L. O. Baksmaty, H. Lu, C. J. Bolech, and H. Pu, Phys. Rev. A **83**, 023604 (2011).

[29] H. Lu, L. O. Baksmaty, C. J. Bolech, and H. Pu, Phys. Rev. Lett. **108,** 225302 (2012).

[30] M. W. Zwierlein, A. Schirotzek, C. H. Schunck, and W. Ketterle, Science **311**, 492 (2006).

[31] M. W. Zwierlein et al., Nature(London) **442**, 54 (2006).

[32] C. H. Schunck et al., Science **316,** 867 (2007)

[33] I. Y. Shin et al., Nature **451,** 689 (2008)

[34] G. B. Partridge, W. Li, R. I. Kamar, Y. A. Liao, and R. G. Hulet, Science **311**, 503 (2006).

[35] G. B. Partridge, W. Li, Y. A. Liao, and R. G. Hulet, M. Haque and H. T. C. Stoof, Phys. Rev. Lett. **97**, 190407 (2006).

[36] C. Lobo, A. Recati, S. Stringari Phys. Rev. Lett. **97**, 200403 (2006).

[37] S. Pilati, S. Giorgini, Phys. Rev. Lett. **100**, 030401 (2008).

[38] K. B. Gubbel, H. T. C. Stoof, Phys. Rev. Lett. **100**, 140407 (2008).

[39] X.-J Liu, H. Hu and P. Drummond, Phys. Rev. A **75,** 023614 (2007)

[40] S. Nascimbne, N. Navon, K. J. Jiang, L. Tarruell, M. Teichmann, J. McKeever, F. Chevy, and C. Salomon, Phys. Rev. Lett. **103**, 170402 (2009).

[41] D. T. Son, arXiv:0707.1851 (2007)

[42] T. N. De Silva, E. J. Mueller, Phys. Rev. Lett. **97**, 070402 (2006)

[43] M. Haque, H. T. C. Stoof, Phys. Rev. Lett. **98**, 260406 (2007)

[44] Stefan K. Baur, Sourish Basu, Theja N. De Silva, and Erich J. Mueller, Phys. Rev. A **79**, 063628 (2009)

[45] P. De Gennes, Superconductivity of Metals and Alloys, (Addison-Wesley, Reading, MA) (1989)

[46] K. Mizushima, K. Machida and M. Ichioka, Phys. Rev. Lett. **94**, 060404 (2005).

[47] Y. Ohashi and A. Griffin, Phys. Rev. A **72,** 013601 (2005).

[48] J. Kinnunen, L. M. Jensen and P. Torma, Phys. Rev. Lett. **96,** 110403 (2010).

[49] M. Tezuka, Y. Yanase and M. Ueda, preprint arXiv:0811.1650v3

[50] M. M. Parish and D. Huse, Phys. Rev. A **80,** 063605 (2009).

[51] Y. A. Liao, M. Revelle, T. Paprotta, A. S. C. Rittner, W. Li, G. B. Partridge, and R. G. Hulet, Phys. Rev. Lett. **107,** 145305 (2011).

[52] S. Gupta, Z. Hadzibabic, M. W. Zwierlein, C. A. Stan, K. Dieckmann, C. H. Schunck, E. G. M. van Kempen, B. J. Verhaar and W. Ketterle, Science **300,** 1723 (2003).

[53] A. Schirotzek et al., Phys. Rev. Lett. **102,** 230402 (2009).

[54] R. B. Lehoucq, D. C. Sorensen, and C. Yang, ARPACK Users' Guide: Solution of Large-Scale Eigenvalue Problems with Implicitly Restarted Arnoldi Methods. SIAM, Philadelphia (1998).

[55] H. Zhang et al., ACM Trans. Math. Software **33,** 9 (2007).

[56] D. D. Johnson, Phys. Rev. B **38,** 12807 (1988).

[57] T. N. De Silva and E. J. Mueller, Phys. Rev. A **73,** 051602(R) (2006)

[58] A. Imambekov, C. J. Bolech, M. Lukin, and E. Demler, Phys. Rev. A **74**, 053626 (2006)

[59] A. Bulgac and M. M. Forbes, Phys. Rev. Lett. **101,** 215301 (2008)

[60] X. J. Liu, H. Hu, and P. Drummond,Phys. Rev. A **76** 043605, (2007).

[61] G. Orso, Phys. Rev. Lett. **98,** 070402 (2007).

[62] H. Hu, X-J. Liu and P. Drummond, Phys. Rev. Lett. **98,** 070403 (2007).

[63] M. M. Parish, F. M. Marchetti, A. Lamacraft, B. D. Simons, Nature Phys. **3**, 124 (2007).

[64] D. E. Sheehy, L. Radzihovsky, Phys. Rev. Lett. **96**, 060401 (2006).

[65] M. M. Parish,S. K. Baur, E. J. Mueller, and D. Huse, Phys. Rev. Lett. **99**, 250403 (2007).

[66] A. E. Feigun, and F. Heidrich-Meisner, Phys. Rev. B **76** 220508(R), (2007).

[67] M. Casula, D. M. Ceperley, and E. J. Mueller, Phys. Rev. A **7**8,033607 (2008).

[68] M. Tezuka and M. Ueda, Phys. Rev. Lett. **100**, 110403 (2008).

[69] X. W. Guan, M. T. Batchelor, C. Lee, and M. Bortz, Phys. Rev. B **76**, 085120 (2007).

[70] J. Y. Lee, and X. W. Guan, Nucl. Phys. B **853**, 125 (2011).

[71] J. Kajala, F. Massel, and P. Torma, Phys. Rev. A **84**, 041601 (2011).

[72] P. Kakashvili, and C. J. Bolech, Phys. Rev. A **7**9, 041603 (2009).

[73] C. A. Regal, M. A. Greiner, and D. S. Jin, Phys. Rev. Lett. **92**, 040403 (2004).

[74] M. Olshanii, Phys. Rev. Lett. **81**, 938 (1998).

[75] G. Vidal, Phys. Rev. Lett., **91**, 147902 (2003)

[76] G. Vidal, Phys. Rev. Lett. **93**, 040502 (2004).

[77] Finite temperature cannot be readily dealt with in TEBD. However, we performed finite-temperature calculations using BdG and found no qualitative difference as long as the system remains in a superfluid phase.

[78] S.R. White, Phys. Rev. Lett. **69**, 2863 (1992).

[79] R. Horodecki, P. Horodecki, M. Horodecki, and K. Horodecki, Rev. Mod. Phys. **81**, 865 (2009).

[80] A. J. Daley, C. Kollath, U. Schollẅock, and G. Vidal, J. Stat. Mech. P04005 (2004).

[81] http://physics.mines.edu/downloads/software/tebd/.

[82] M. P. Zwolak, Dynamics and simulation of open quantum systems, PhD thesis, California Institute of Technology (2008).

[83] M. Suzuki, Physics Letters A, **146**, 319 (1990).

[84] A. J. Daley. Manipulation and simulation of cold atoms in optical lattices. PhD thesis, Leopold-Franzens Universitat Innsbruck (2005).

[85] M. Tezuka, and M. Ueda, New J. Phys. **12**, 055029 (2010).

[86] K. Yang, Phys. Rev. Lett. **95**, 218903 (2005).

[87] C. Kollath, and U. Schollwock, New J. Phys. **8**, 220 (2006).

[88] E. Zhao, and V.W. Liu, Phys. Rev. A **78**, 063605 (2008).

[89] M. Rizzi et al., Phys. Rev. B **77**, 245105 (2008).

[90] The clear reminiscent of the peaks at finite momentum can be observed till $t = 0.06$ in our result for $g_{1D} = -8$ and $N = 40$.

[91] V. Gritsev, E. Demler, and A. Polkovnikov, Phys. Rev. A **78**, 063624 (2008).

[92] H. Hu, and X.-J. Liu, Phys. Rev. A **83**, 013631 (2011).

[93] M. Swanson, Y. L. Loh, and N. Trivedi, arXiv:1106.3908.

[94] P. D. Lett, R. N. Watts, C. I. Westbrook, W. D. Phillips, P. L. Gould, and H. J. Metcalf, Phys. Rev. Lett. 61, 169 (1988).

[95] I. Bloch, J. Dalibard, and W. Zwerger, Rev. Mod. Phys. 80, 885 (2008).

[96] G. Bruun, Y. Castin, R. Dum, and K. Burnett, Eur. Phys. J. D **7**, 433-439 (1999).

[97] T. Busch, B. G. Englert, K. Rzazewski, and M. Wilkens, Found. Phys. **28**, 549 (1998).

[98] M. D. Girardeau and G. E. Astrakharchik, Phys. Rev. A **81**, 061601 (2010).

[99] M. D. Girardeau, Phys. Rev. A **82**, 011607 (2010).

[100] F. Serwane, G. Zrn, T. Lompe, T. B. Ottenstein, A. N. Wenz, and S. Jochim, Science **332**, 336 (2011).

[101] G. Zurn, F. Serwane, T. Lompe, A. N. Wenz, M. G. Ries, J. E. Bohn and S. Jochim, Phys. Rev. Lett. **108**, 075303 (2012).

[102] M. G. Benedict, J. Kovacs, and A. Czirjak, J. Phys. A: Math. Theor. **45** 085304 (2012)

[103] K. Sun, and C.J. Bolech, Phys. Rev. A **85**, 051607(R) (2012).